



# **Vital Signs Monitoring: Breathing Rate and Heartbeat Rate Detection**

Aaron Tekleab

M.Sc. Thesis

December 2022

A thesis submitted to Khalifa University of Science and Technology in accordance with the requirements of the degree of M.Sc. in Electrical and Computer Engineering in the Department of Electrical Engineering and Computer Science.



# **Vital Signs Monitoring: Breathing Rate and Heartbeat Rate Detection**

by

**Aaron Tekleab**

A thesis submitted in partial fulfillment of the  
requirements for the degree of

**M.Sc. in Electrical and Computer Engineering**

at

**Khalifa University**

**Thesis Committee**

Dr. Mihai Sanduleanu (Main Advisor),  
*Khalifa University*

Dr. Baker Mohammad (Co-Advisor)  
*Khalifa University*

Prof. Mahmoud Al-Qutayri (RSC member 1),  
*Khalifa University*

Dr. Hani Saleh (RSC member 2)  
*Khalifa University*

December 2022

# Abstract

Aaron Tekleab, “**Vital Signs Monitoring: Breathing Rate and Heartbeat Rate Detection**”, M.Sc. Thesis, M.Sc. in Electrical and Computer Engineering, Department of Electrical Engineering and Computer Science, Khalifa University of Science and Technology, United Arab Emirates, December 2022.

The Healthcare sector has been hugely impacted by the emergence of non-contact vital signs detection technology. Substituting contact-based vital signs monitoring devices with wireless devices has attracted the attention of the healthcare industry. The frequency-modulated continuous wave (FMCW) radar has recently dominated the literature and has shown a promise to realize the measurement of vital signs remotely. However, the sole reason that prevents wireless technology from replacing standard devices is accuracy. To overcome this, radars with high operating frequencies and large bandwidths are required. These features give the radars high resolution to detect small displacement changes in the order of the sub-millimeter range. Radars of such features require complex hardware architectures and efficient signal processing algorithms.

In this work, an efficient algorithm has been prepared for a state-of-the-art vital sign monitoring FMCW radar that operates at 160 GHz frequency with 10 GHz bandwidth that was designed by Khalifa University of Science and Technology (KUST). The algorithm uses phase-based measurement to detect and estimate the vital signs of a subject. The algorithm further addresses the IQ imbalances caused by hardware imperfections that affect vital measurements. It deploys compressed sensing-based signal reconstruction and wavelet decomposition algorithms which recent papers have claimed to have scored higher accuracy compared to other monitoring algorithms. However, since the measurement of the FMCW radar designed in KUST was not finished, the algorithm was validated using a public dataset that was acquired using FMCW radar manufactured by Texas Instruments. The performance of the algorithm was then compared with vital rates acquired using a clinically approved vital signs monitoring device called Nihon Kohden which was synchronized with the FMCW radar during data acquisition.

This work also addresses the measurement setup for the transmitter and receiver blocks of the radar IC designed in KUST. The challenges of measuring devices operating at high frequencies are also discussed. Moreover, the connection setup of the boards that are to be used to capture the intermediate frequency (IF) signal is also covered. The setup was successfully tested, and it will be used with the radar IC measurement in the future.

**Indexing Terms:** vital signs, FMCW radar, fast Fourier transform, filtering, compressed sensing, wavelet decomposition, AD9082, ADS9-V2EBZ

# Acknowledgment

I would like to express my deepest gratitude to my supervisor Dr. Mihai Sanduleanu for his invaluable support, supervision, and guidance throughout my thesis project. I would also like to extend my sincere thanks to my co-advisor Dr. Baker Mohammad and RSC members, Prof. Mahmoud Al-Qutayri and Dr. Hani Saleh, who generously provided constructive ideas and feedback. Moreover, I would like to acknowledge Dr. Solomon Serunjogi and Dr. Ademola Akeem for their support during measuring the Radar IC and Dr. Temesghen Habte and Dr. Mizan Gebremicheal for sharing their knowledge and expertise that saw me successfully finish my project.


Lastly, I would be remiss in not mentioning my close friends and my family. Their belief in me has kept my motivation and spirit high during this journey.

# Declaration and Copyright

## Declaration

I declare that the work in this thesis was carried out in accordance with the regulations of Khalifa University of Science and Technology. The work is entirely my own except where indicated by special reference in the text. Any views expressed in the thesis are those of the author and in no way represent those of Khalifa University of Science and Technology. No part of the thesis has been presented to any other university for any degree.

Author Name: Aaron Zerai Tekleab

Author Signature: \_\_\_\_\_

Date: 12/12/2022

## Copyright ©

No part of this thesis may be reproduced, stored in a retrieval system, or transmitted, in any form or by any means, electronic, mechanical, photocopying, recording, scanning or otherwise, without prior written permission of the author. The thesis may be made available for consultation in Khalifa University of Science and Technology Library and for inter-library lending for use in another library and may be copied in full or in part for any bona fide library or research worker, on the understanding that users are made aware of their obligations under copyright, i.e., that no quotation and no information derived from it may be published without the author's prior consent.

# Contents

<b>Abstract.....</b>	<b>ii</b>
<b>Acknowledgment.....</b>	<b>iii</b>
<b>Declaration and Copyright.....</b>	<b>iv</b>
<b>Contents .....</b>	<b>v</b>
<b>List of Figures.....</b>	<b>vii</b>
<b>List of Tables .....</b>	<b>viii</b>
<b>Chapter 1: Introduction .....</b>	<b>1</b>
<b>1.1. Radar Systems .....</b>	<b>1</b>
<b>1.1.2. Working Principles of FMCW Radar for Vital Signs Detection .....</b>	<b>2</b>
<b>1.2. Motivation and Challenges.....</b>	<b>5</b>
<b>1.3. Objectives.....</b>	<b>6</b>
<b>1.4. Contributions.....</b>	<b>6</b>
<b>1.5. Thesis Outline .....</b>	<b>7</b>
<b>Chapter 2: Literature Review.....</b>	<b>8</b>
<b>Chapter 3: Dataset, Proposed Algorithm, and Implementation.....</b>	<b>11</b>
<b>3.1. Dataset.....</b>	<b>11</b>
<b>3.2. Algorithm Flow Chart .....</b>	<b>12</b>
<b>3.2.1. I-Q Imbalance Correction Using S.W. Ellingson Algorithm .....</b>	<b>12</b>
<b>3.2.2. FFT Algorithm and Estimation of Target Range.....</b>	<b>14</b>
<b>3.2.3. Phase Extraction, Differential Phase, and Impulse Noise Removal .....</b>	<b>16</b>
<b>3.2.4. Filtering Based Vital Signs Estimation .....</b>	<b>18</b>
<b>3.2.5. Compressed Sensing Based Signal Reconstruction.....</b>	<b>19</b>
<b>3.2.6. Wavelet Decomposition .....</b>	<b>21</b>
<b>3.3. Performance Analysis .....</b>	<b>23</b>
<b>Chapter 4: Hardware Radar IC Measurement.....</b>	<b>25</b>
<b>4.1. Measuring the Tx and Rx Antennas.....</b>	<b>25</b>
<b>4.1.1. Measuring the Receiver: Transmitter Block .....</b>	<b>25</b>
<b>4.1.2. Measuring the Transmitter: Receiver Block .....</b>	<b>26</b>

4.1.3.    Biasing the IC .....	27
4.2.    ADC and ADS9-V2EBZ Evaluation Board .....	28
<b>Chapter 5: Conclusion and Future Work.....</b>	<b>31</b>
5.1.    Conclusion.....	31
5.2.    Future Work .....	32
<b>Bibliography .....</b>	<b>33</b>
<b>Appendices.....</b>	<b>36</b>
<b>Appendix A: Algorithm Codes.....</b>	<b>36</b>
i.    S.W. Ellingson Algorithm.....	36
ii.   Range – FFT Algorithm.....	36
iii.  Peak Frequency Detection .....	37
iv.   Range Calculation.....	37
v.    Range bin Selection .....	38
vi.   Phase Extraction.....	39
vii.  Phase Difference .....	39
viii. Impulse Noise Removal .....	40
ix.   Filter Design.....	41
x.    Autocorrelation based Estimation.....	41
xi.   CS based Signal Reconstruction .....	42
xii.  Wavelet Decomposition .....	43

# List of Figures

Figure 1: Chirp Signal .....	2
Figure 2: Mixer properties - Frequency vs Time plot.....	3
Figure 3: Detecting, ranging, and chest modeling [9] .....	5
Figure 4: Common Vital Signs Extraction Algorithm.....	9
Figure 5: Modified Algorithm Flow Chart [23] .....	12
Figure 6: Correcting I-Q Imbalance .....	14
Figure 7: range-FFT operation.....	15
Figure 8: Range-FFT (Range Profile).....	15
Figure 9: Extracted IF signal Phase .....	17
Figure 10: Differential Phase Signal before and after denoising .....	18
Figure 11: Filter outputs .....	18
Figure 12: CS-OMP Reconstructed Breathing Signal .....	20
Figure 13: CS-OMP Reconstructed Heartbeat Signal .....	21
Figure 14: Filtering property of the Wavelet Decomposition .....	22
Figure 15: Wavelet Decomposition Output.....	22
Figure 16: Transmitter Setup .....	25
Figure 17: Transmitted Signal Phase Noise.....	25
Figure 18: Receiver Setup .....	26
Figure 19: Acquired IF Signal .....	27
Figure 20: Radar IC Biasing Circuitry.....	27
Figure 21: ADC and the Evaluation Board Setup .....	28
Figure 22: ADC and Evaluation Board Setup Test Configuration .....	29
Figure 23: Transmitted and Captured Data .....	30



# List of Tables

Table 1: IWR-6843 Radar Parameters and Setup.....	11
Table 2: Breathing rate and Heartbeat rate estimations.....	23

# Chapter 1: Introduction

## 1.1. Radar Systems

Radio detection and ranging (Radar) was first developed for detecting and tracking massive mobile targets at large distances. For instance, air-defense radar systems and marine radars [1]. The transportation industry inherited the use of radars to detect the range of vehicles from radars and their respective velocity [2]. Short distance ranging and small displacement sensing became viable with the emergence of millimeter wave (mm-wave) radars. Several research sectors showed interest in these radars such as the automotive, agriculture, and biomedical sectors. The biomedical sector adopted mm-wave radars to monitor vital signs by tracking and modeling the physiological movements of the chest wirelessly. The chest movement model is then processed to acquire vital signs: breathing rate and heartbeat rate [1], [3]. Wireless vital signs detection opened potential applications that were not possible before such as continuous monitoring of patients without any contact and predicting and preventing severe heart and lung-related health issues, for instance, sleep apnea [1], [4], [5]. Moreover, multiple people can be monitored simultaneously using multiport radar systems [6], [7]. Other than medical applications, wireless vital sign detection radars are also used to detect human beings in rescue missions in earthquake-affected areas or soldiers on a battlefield [1].

Due to easier portability, easier integration, and applicability in situations where contact-based monitoring is impossible, wireless vital sign detection features the potential of replacing the standard contact-based vital sign monitoring devices [6]. Currently, three main kinds of radar architectures are used in the biomedical sector. These are continuous wave doppler radar, impulse-radio ultra-wideband (IR-UWB) radar, and frequency-modulated continuous wave (FMCW) radar [3], [4].

CW doppler radar operates by emitting a single-tone continuous wave signal to obtain the phase information of the target from which the vital signs are retrieved. CW signals possess high power that enables them to travel long distances. However, a single-tone wave lacks bandwidth which means the CW doppler radar does not possess range resolution [4]. Range resolution determines the precision of the radar in discriminating closely placed targets or the target from nearby interference. Range resolution is directly proportional to the bandwidth of the transmitted signal. On contrary, IR-UWB radar transmits impulses with large bandwidth. Therefore, this radar can detect small movements of the target and discriminates the target from nearby clutter. However, being transmitted in narrow impulses degrades the distance coverage capability of the radar. Moreover, phase-based measurement cannot be performed on non-continuous wave radars. Recent research papers note that phase-based measurement results in high precision in vital sign detection. Based on the aforementioned radars, the fundamental radar feature necessary for precise and accurate vital sign detection is transmitting CW multitone signal.

This is the main reason why FMCW radar dominates the current literature on wireless vital signs detection.

FMCW embraces the strengths of both CW doppler and IR-UWB radars and overcomes their shortcomings. It operates using a CW signal with finite bandwidth. CW signal possesses high energy and propagates a longer range, and it increases the signal-to-noise ratio (SNR) of the signal received. The finite bandwidth enables the radar to isolate the target from nearby interferences. Moreover, FMCW radar is robust because the vital sign information is extracted from the received signal's phase. Thus, noise has less impact on FMCW radar compared to impulse radar where the vital signs are extracted from amplitude [8]. Vital signs detection is performed via phase-based measurement which increases the precision and accuracy of the results. In this thesis project, a FMCW radar-recorded dataset will be the basis for analyzing the algorithm written for vital signs detection. Hardware measurements for the receiver and transmitter blocks of a state-of-the-art 160 GHz FMCW radar integrated circuit (IC) designed in KUST will also be discussed. The following section will cover the basic working principles of the FMCW radar for vital signs detection and estimation.

### 1.1.2. Working Principles of FMCW Radar for Vital Signs Detection

The working basis of all radar systems is that the transmitter antenna emits an electromagnetic wave that interacts with the target and is reflected to the receiver antenna. The received signal is processed to reveal the range and vital signs information of the target. The FMCW radar transmits a signal called a chirp. A chirp is a sinusoidal signal whose frequency increases linearly with time. Figure 1 (a) shows the frequency and time properties of the chirp signal and (b) shows the sinusoidal signal in the time domain.

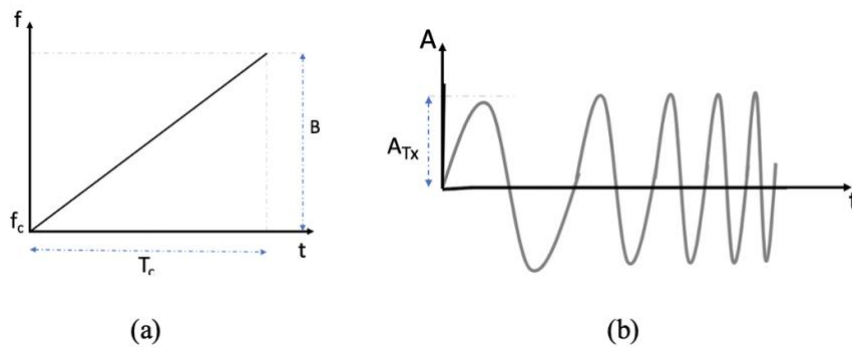


Figure 1: Chirp Signal

A chirp is modeled using the following mathematical equation and has a quadratic time relationship:

$$S_{Tx} = A_T \cos \left( 2\pi f_c t + \pi * \frac{B}{T_c} t^2 + \phi(t) \right) \quad (1)$$

where  $A_T$  is the transmitted power,  $f_c$  is the minimum chirp frequency,  $B$  is the bandwidth,  $T_c$  is the chirp duration, and  $\phi(t)$  is the transmitted signal phase shift.

Once the transmitted signal encounters a target, it echoes back to the receiver antenna with a propagation delay,  $T_d$ , whose value is  $\frac{2d}{c}$  where  $d$  is the target distance from the antenna and  $c$  is the speed of light. Therefore, the same mathematical model is used for the received signal as shown in equation (2), but the power is attenuated and time is delayed:

$$S_{Rx} = \alpha A_T \cos \left( 2\pi f_c(t - T_d) + \pi * \frac{B}{T_c}(t - T_d)^2 + \phi(t - T_d) \right) \quad (2)$$

$\alpha$  is the power attenuation factor and  $T_d$  is the propagation delay. The received signal is then mixed with the transmitted signal to acquire the intermediate frequency (IF) signal. A mixer outputs a signal whose frequency is the difference of the frequencies of the two input signals and whose phase is the difference of the phases of the two input signals. The relationship between the inputs,  $S_{Tx}$  and  $S_{Rx}$ , and the output i.e., the IF signal of the mixer can be demonstrated using a frequency-time plot in Fig. 2.

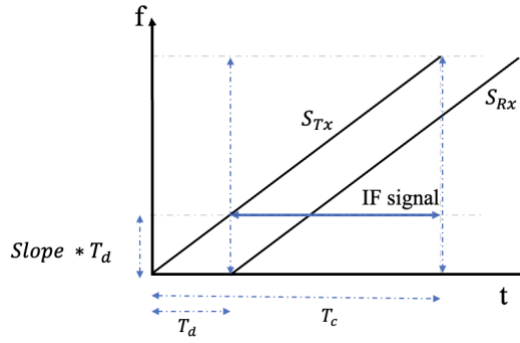


Figure 2: Mixer properties - Frequency vs Time plot

As observed from Fig. 2, the IF signal is of a constant frequency whose value is the product of the transmitted signal's slope and the propagation delay. The mathematical operation of the mixer can be shown as:

$$\begin{aligned} S_{IF} &= S_{Tx}(t)S_{Rx}^*(t) \\ &= \frac{\alpha A_{Tx}^2}{2} \cos \left( \left( 2\pi f_c t + \pi * \frac{B}{T_c}(t)^2 + \phi(t) \right) - \left( 2\pi f_c(t - T_d) + \pi * \frac{B}{T_c}(t - T_d)^2 + \phi(t - T_d) \right) \right) \\ &= \frac{\alpha A_{Tx}^2}{2} \cos \left( 2\pi f_c T_d - \frac{\pi B T_d^2}{T_c} + \frac{\pi B 2t T_d}{T_c} + \phi(T_d) \right) \end{aligned} \quad (3)$$

From the above derivation, it is observed that the IF signal's frequency and its phase respectively are:

$$f_{IF} = \frac{B T_d}{T_c} = \frac{2Bd(\tau)}{c * T_c} \quad \phi_{IF} = 2\pi f_c T_d = \frac{4\pi f_c d(\tau)}{c} \quad (4)$$

The second phase component of  $S_{IF}$  in equation (3) is called residual video phase (RVP) and since  $T_d$  is within microseconds range, RVP is negligible and can be ignored [4]. And the fourth term  $\phi(T_d)$  is directly proportional to the target distance and for short-range applications such as vital sign detection, it is negligible and can also be ignored [6].

Both  $f_{IF}$  and  $\phi_{IF}$  are dependent on the target range thus target range can be found either by finding the IF signal's frequency or its phase. The simplest approach would be performing the Fast Fourier Transform (FFT) operation on the IF signal which transforms the time domain signal to the frequency domain. This reveals the IF signal frequency, and the range of the target can be found by:

$$d(\tau) = c * \frac{T_c * f_{IF}}{2B} \quad (5)$$

N.B.  $\tau$  represents the slow time component of the signal. Fast time refers to the time associated with the sampling rate of the analog-to-digital converter (ADC) whereas slow time is the real-world time i.e., it represents the chirp transmission time. Therefore, the range depends on slow time. For a single chirp transmission, the chest is assumed to stay still in one position. This is because the chirp propagation takes microseconds and for the chest to displace by 1 mm, it has to move at a very high velocity. Thus, it is reasonable to assume the chest shows insignificant displacement change during a single chirp transmission. If there are multiple objects in front of the radar, multiple IF signals are received and multiple peaks are displayed on the frequency spectrum of the IF signal. As mentioned before, the range resolution is the ability of the radar to segregate closely placed objects. Objects that are placed close to each other separated by a distance that is less than the range resolution of the radar are displayed as a single peak in the frequency spectrum. The range resolution is calculated using the following equation:

$$d_{res} = \frac{c}{2B} \quad (6)$$

To find the rate of displacement change of the chest using  $\frac{\Delta d(\tau)}{T_c}$ , more than one chirp is required. However, the chest displacement change is in millimeters, and it is much less than the range resolution. Thus, no change is observed in the frequency spectrum of consecutive chirps which hinders the use of the previously mentioned method. However, the phase of consecutively received chirps shows a significant change, and the rate of displacement change of the chest can be measured from the phase of the IF signal. The chest movement can be modeled as a sinusoid and phase-based measurement results in a similar output. In summary, the subject detection and ranging will be achieved using the IF signal's frequency and the chest movement modeling will be done using the phase of the IF signal as shown in Fig. 3. The vital signs can then further be processed from the model.

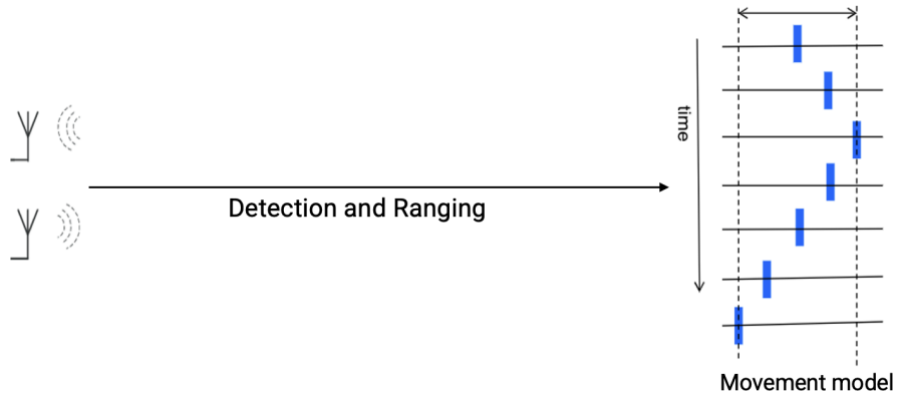


Figure 3: Detecting, ranging, and chest modeling [9]

## 1.2. Motivation and Challenges

As discussed before, wireless vital signs detection and estimation has caught the attention of the biomedical industry. And it has proven to be crucial in scenarios where the standard vital signs detection devices cannot be applied, for instance, it can be used to measure the vital signs of burn victims [10] and of those who have skin allergies [11]. Moreover, its ability to detect and measure the vital signs of multiple targets simultaneously [12] and its ability to be integrated with artificial intelligence and advanced prediction algorithms to detect heart and lung-related abnormalities at early stages has bolstered its significance in the biomedical sector [13]–[15]. However, technology comes with some challenges. From the signal processing perspective, the heartbeat signal’s amplitude is small and is comparable with noise amplitudes. Breathing signal harmonics also add complexity in isolating and detecting the heartbeat signal. Thus, the vital signs detection algorithm should address these issues. From the hardware design perspective, the FMCW radar needs to have high bandwidth for better range resolution. Higher operating frequency is also desirable as carrier wavelength is inversely proportional to the phase change due to the chest movement which results in more precise heartbeat signal detection [15]. Therefore, complex architecture designs are required due to various reasons such as behavior change of passive elements at high frequencies and high sensitivity to external and internal noise [16]. Measurements in radio frequency (RF) also requires high-frequency equipment and wires. The equipment in the lab might not be of high-frequency range therefore devices such as mixers have to be used to meet the desired frequency ranges. The system is susceptible to internal and external noise, and wires and connectors result in signal power attenuation thus amplifiers might be used as well to satisfy the power requirement of components.

### 1.3. Objectives

The objectives of this thesis project are

- i) to develop an algorithm that estimates the breathing rate and heartbeat rate accurately by addressing the issues that have been discussed in section 1.2. It is expected the estimations to be close to the rates recorded by a clinically approved sensor.
- ii) to measure the predesigned vital signs monitoring radar IC. To measure the chip, signal transmission and reception have to be confirmed first. Therefore, antenna measurement is performed. Then, the chip is tested as one entity. If the chip measurement fails to acquire the desired signal, the different components of the chip are to be examined one by one for faults.
- iii) to integrate and configure the boards that are used for capturing and sampling the IF signal. The IF signal is processed using MATLAB thus the boards have to be configured to connect to MATLAB.

Once those three objectives are achieved, they are to be integrated and get tested on actual human targets.

### 1.4. Contributions

The main contributions of this research can be summarized as follows:

- Present a detailed overview of the prepared algorithms and their significance for the project. Each algorithm is explained along with its derivations, and its respective code is provided in the appendix section.
- Implementation and comparison of three popular vital sign detection and estimation algorithms that currently are of interest in the literature. Their performance will be analyzed using the child dataset acquired from [17].
- Transmitter and receiver measurement blocks are set up for measuring the receiver and transmitter blocks of the vital signs FMCW radar IC respectively.
- Configuration and integration of the boards, AD9082 and ADS9 evaluation boards, which are to be used for capturing the IF signal from the radar IC. These boards are configured to remotely capture the IF signal and copy the samples to the host computer for processing.

## 1.5. Thesis Outline

Chapter 2 will discuss the current related work done in the field of FMCW radar technology with a focus on signal processing algorithms for vital signs monitoring. Various algorithms proposed by different papers alongside their drawbacks will be examined.

Chapter 3 will focus on the flow of the algorithms that were used in this project. The role of those algorithms and their derivations, implementations, and experimental results are discussed. At the end of the chapter, the performance of the algorithm will be analyzed by comparing it to a dataset acquired by a clinically approved device.

Hardware measurements of the radar IC alongside with configuration of the AD9082 and ADS9-V2EBZ boards with MATLAB will be covered in chapter 4. The transmitter and receiver measurement setups and their challenges will be discussed here. The setups will be tested, and the results will be covered in this chapter as well.

Finally, the conclusion and intended application of this algorithm on a state-of-the-art chip will be discussed in the future work section of chapter 5. The main algorithms' snippets will also be provided in the appendices.



## Chapter 2: Literature Review

[9] explained the basic principles of FMCW radars. The author discussed the working principles of radars and the common algorithms that are used to find the range, speed, and vibration rate of the target. The importance of phase-based measurement in detecting small vibrations is also illustrated. Differentiating vital signs of equidistant multiple targets from the radar and angular measurement for absolute ranging are also discussed. [4] and [18] clarified the differences between the common radar kinds that are currently being used for detecting vital signs. [4] explained why the FMCW radar dominates the current literature. [4] and [18] also explained the role of the transmitter and receiver architectures in signal acquisition and its quality. The desired features of various components such as the antennas, mixer, and ADC were discussed. Phase-based measurement was deployed in both papers. Arctangent algorithm was used for phase demodulation and its shortcomings and how to address those issues were also explained. The breathing rate and heartbeat rate were then acquired by filtering the unwrapped phase preceded by clutter-corrupted data segment removal.

Even though [4] explained the superiority of FMCW radar, [3] compared FMCW radar and IR-UWB radar experimentally and found out that IR-UWB radar achieved the same accuracy and even scored higher SNR than the FMCW radar. Both papers deployed similar algorithms and the results of the radars for [3] were compared with medically approved devices: respiration belt and ECG sensor. The authors of [19] and [20] used the same procedure as [4] to obtain the target range and phase. Gaussian low pass filter was used to smooth the unwrapped phase signal and segregate the breathing signal. The breathing rate was acquired by using a peak detection algorithm in the time domain. However, the same method as [4] couldn't be used to estimate the heartbeat rate due to the presence of the breathing signal's harmonics and noise. Therefore, [19] proposed FFT alike but an advanced method that breaks down the signal into intrinsic functions known as the empirical mode decomposition (EMD). After the time-domain signal decomposition, an independent component analysis followed by peak detection was proposed to obtain the heartbeat rate. However, the authors couldn't implement the proposed algorithm because of its implementation complexity. They instead deployed a harmonic filter to suppress the breathing harmonics and a bandpass filter to obtain the heartbeat signal. For a 1-meter positioned target, 90.48% and 90.54% accuracy were achieved for breathing rate and heartbeat rate respectively.

[6] also implemented the same method as [19] but used gaussian interpolation after doppler FFT to estimate the vital signs. The authors also explained the impact of phase noise and its relationship with range and the importance of removing DC distortion before phase computation. The experiment achieved 94% and 80% accuracy for breathing rate and heartbeat rate estimations respectively. [21] proposed using Bessel functions for peak detection using doppler radar. However, the main drawback of the implementation was that the heartbeat signal was undetectable unless the target holds his/her

breath. [9] explained the significance of the number of samples in FFT. Thus, [22] zero-padded the intermediate frequency signal to increase the accuracy in frequency components. The authors used bandpass filters to obtain the vital sign signals followed by doppler FFT to estimate the breathing and heartbeat rates. Having prior knowledge of the target location, the authors already knew which range bin to select. [10] deployed two radars of 2.4 GHz and 24 GHz operating frequencies and compared their performance. Phase-based measurement was used, and the arctan algorithm was implemented to extract the phase followed by bandpass filtering of the unwrapped phase to get the vital signs. Autocorrelation was performed for spectral estimation to increase the periodicity of the signal. The radar with a 2.4 GHz operating frequency resulted in 2.35% and 8.24% errors for breathing rate and heartbeat rate respectively while the second radar resulted in 1.85% and 6.17% errors for breathing rate and heartbeat rate respectively.

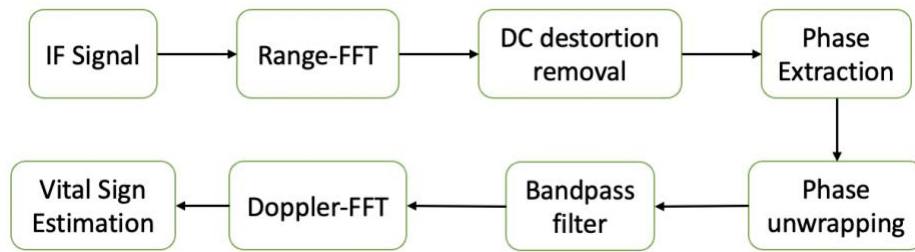


Figure 4: Common Vital Signs Extraction Algorithm

Figure 3 is the basis for the signal processing section of the above-mentioned papers. Range-FFT extracts the IF frequency and is used to evaluate the target location, then DC compensation is performed to remove DC offset. The classic algorithm for phase demodulation, the arctan algorithm was deployed by all the papers followed by phase unwrapping. A bandpass filter is then used to separate the vital signs, and, in some papers, a harmonic filter was used to suppress breathing signal harmonics. Vital signs were estimated either in the time domain via autocorrelation and peak detection or in the frequency domain by performing doppler-FFT followed by peak detection.

[5], [23], [24], and others to be discussed later highlighted the drawbacks of the above flowchart in measuring the heartbeat rate and deployed more advanced signal processing mechanisms. [23] and [24] found the differential phase by subtracting consecutive elements of the phase signal to enhance the heartbeat signal. [24] also used a gain control algorithm to either correct or remove motion-corrupted segments. The gain control algorithm reduced the impact of large amplitude movements on the heartbeat signal. [5] used wavelet transformation to extract the heartbeat rate from a doppler radar without the need to filter the differential phase. Wavelet transformation gives detailed information on the frequency components of a signal. [23] implemented a phase demodulation mechanism that does not result in a wrapped phase. The authors deployed the differential and cross-multiplication (DACM) algorithm followed by differential phase operation. Filtering followed by compressed sensing is then used to

estimate the breathing rate and discrete wavelet decomposition on the differential phase is used to estimate the heartbeat rate. The strengths and drawbacks of each algorithm are also explained. Authors of [25] also claimed that random body movements can be dealt with by finding the difference of two-phase signal from collocated two receiver antennas. [26] and [27] stressed the effects of noise interference and the interference of breathing signal harmonics on the heartbeat signal. The authors proposed variational mode decomposition (VMD) and wavelet transformation. VMD is used to decompose the vital signals into intrinsic mode function components. Desired frequency components with high amplitudes are used to reconstruct the vital signs. A wavelet-based de-noising method is then performed to remove noise from the reconstructed vital signals. The authors claim the proposed method overcomes the influence of breathing harmonics and improves the SNR and detection accuracy of the heartbeat signal.

# Chapter 3: Dataset, Proposed Algorithm, and Implementation

## 3.1. Dataset

The dataset from [17] that was used to validate the proposed algorithm was acquired using Texas Instruments (TI) IWR-6843 FMCW radar. The radar transmits 20 frames per second. Each frame comprises 2 chirp signals of 256 samples each. For processing, only the first chirp of each frame transmitted is used. Moreover, out of the 4 receiver antennas of the radar, the data accumulated by one receiver antenna is used. Table 1 lists the technical features of the radar and the settings that were deployed to accumulate the dataset.

*Table 1: IWR-6843 Radar Parameters and Setup*

Parameter	Value	Used Setting
Number of Transmit Antennas	3	1
Number of Receive Antennas	4	4
Starting Frequency	60 GHz	60.25 GHz
Bandwidth	4 GHz	3.75 GHz
ADC Sampling Rate	-	3 Msps
Chirp duration	-	91.72 $\mu$ sec
Number of chirps per frame	-	2
Frames per second	-	20

The radar transmitted 6000 frames within 300 seconds. The data was organized into a 6000 by 256 matrix for processing. Each row contains samples of each first chirp received per frame. [17] also contained a dataset that was obtained using a clinically approved vital signs sensor, Nihon Kohden BSM6501K. The reference sensor was synchronized with the radar sensor and acquired the actual vital signs data. The sensor uses electrocardiogram (ECG) and transthoracic impedance pneumography techniques to extract the heartbeat rate and breathing rate respectively.

The data accumulated is of 50 children who are below the age of 13. And since most of them are months old, a seat with a seatbelt was used which resulted in clutter. Moreover, children tend to move their bodies which also results in corrupted signals. Therefore, for this project the data of 4 children aged between 9 and 13 years are used. To prevent large movement corrupted data, a dataset accumulated between 20 and 60 seconds was used.

## 3.2. Algorithm Flow Chart

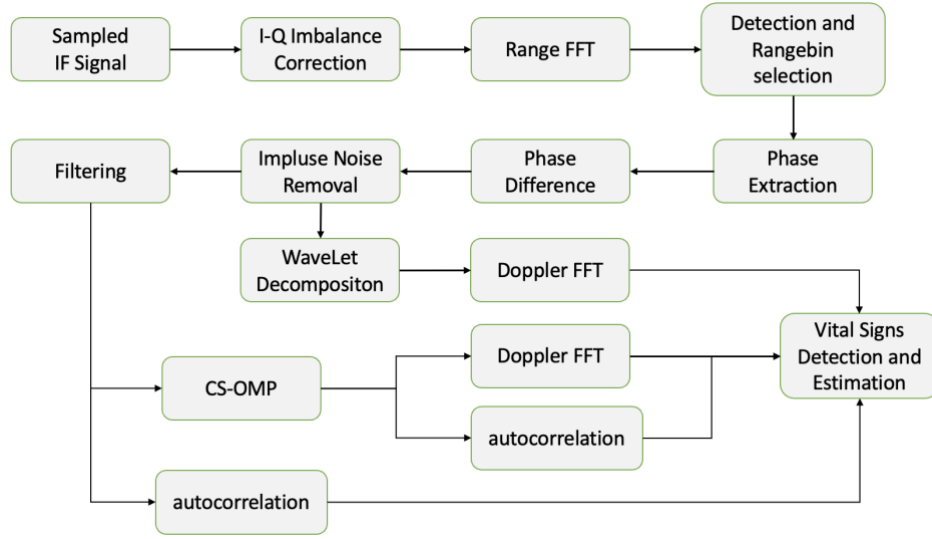


Figure 5: Modified Algorithm Flow Chart [23]

Since the target range is not assumed to be pre-known, the first objective is to find the target location. This is achieved by taking the FFT of the complex IF signal as discussed in section (1.1.2). Ideally, the frequency spectrum of the IF signal shows a single peak frequency at the frequency bin where the target is detected. However, the frequency spectrum might consist of huge spikes in the 0 Hz frequency due to DC offset presence. The reasons for the presence of DC offset can be due to i) antenna coupling or ii) IF signals from stationary part of the body or nearby interference [8] or iii) imbalance between IQ channels [28]. Therefore, before detecting the target location, the DC offset, amplitude imbalance, and phase imbalance issues are addressed. Several algorithms are used to remove the DC offset and correct the amplitude and phase imbalance, for instance, the circular center dynamic DC offset tracking methods. For this project, an algorithm called S.W. Ellingson was used to correct both the DC offset and IQ signals imbalance. Section 3.2.1 discusses the derivation of the algorithm, and more detail is found in [29].

### 3.2.1. I-Q Imbalance Correction Using S.W. Ellingson Algorithm

Ideal I and Q components of the IF signal can be modeled as sine and cosine sinusoids:

$$\begin{aligned} I(t) &= \cos(\omega t) \\ Q(t) &= \sin(\omega t) \end{aligned} \quad (7)$$

However, the realistic models include amplitude and phase imbalance and DC offset. Therefore, the above-given models are updated to:

$$\begin{aligned} I'(t) &= \alpha \cos(\omega t) + \beta_I \\ Q'(t) &= \sin(\omega t + \theta) + \beta_Q \end{aligned} \quad (8)$$

The amplitude imbalance,  $\alpha$ , is reflected on the I signal and the phase imbalance,  $\theta$ , is reflected on the Q signal.  $\beta_I$  and  $\beta_Q$  represent the DC offset values in I and Q signals respectively. The offsets represent the mean of the signals thus, they can easily be removed by subtracting the mean of the received signals from the models above resulting in:

$$I''(t) = \alpha \cos(\omega t) = \alpha * I(t) \quad (9 - a)$$

$$\begin{aligned} Q''(t) &= \sin(\omega t + \theta) \\ Q''(t) &= \sin(\omega t) \cos(\theta) + \cos(\omega t) \sin(\theta) \\ Q''(t) &= Q(t) * \cos(\theta) + I(t) * \sin(\theta) \end{aligned} \quad (9 - b)$$

From the above-derived models, I(t) and Q(t) can be expressed as:

$$\begin{aligned} \begin{bmatrix} I''(t) \\ Q''(t) \end{bmatrix} &= \begin{bmatrix} \alpha & 0 \\ \sin(\theta) & \cos(\theta) \end{bmatrix} \begin{bmatrix} I(t) \\ Q(t) \end{bmatrix} \\ \begin{bmatrix} I(t) \\ Q(t) \end{bmatrix} &= \begin{bmatrix} \alpha^{-1} & 0 \\ \alpha^{-1} \tan(\theta) & \sec(\theta) \end{bmatrix} \begin{bmatrix} I''(t) \\ Q''(t) \end{bmatrix} \end{aligned} \quad (10)$$

By finding  $\alpha$  and  $\theta$ , the correction matrix can be constructed, and this is done by first defining

$$\langle x(t) \rangle = \frac{1}{NT} \int_{t-NT}^t x(u) du \quad (11)$$

where T is the period and N is any positive integer. Based on this definition,

$$\langle I''(t) I''(t) \rangle = \alpha^2 \langle \cos^2(\omega t) \rangle = \alpha^2 \left\langle \frac{1}{2} + \frac{1}{2} \cos(2\omega t) \right\rangle = \frac{1}{2} \alpha^2 \quad (12 - a)$$

Therefore,  $\alpha = \sqrt{2 \langle I''(t) I''(t) \rangle}$ . And following the same procedure on  $\langle I''(t) Q''(t) \rangle$ ;

$$\begin{aligned} \langle I''(t) Q''(t) \rangle &= \frac{1}{2} = \frac{1}{2} \alpha^2 \sin(\theta) \\ \theta &= \sin^{-1} \left( \left( \frac{2}{\alpha} \right) \langle I''(t) Q''(t) \rangle \right) \end{aligned} \quad (12 - b)$$

Thus, by finding  $\alpha$  and  $\theta$  using the derived equations, the near-ideal I-Q signals can be extracted.

Figure 6 (a) shows the unbalanced IQ signals both in waveform and constellation diagrams and Fig. 6 (b) shows the output of the S.W. Ellingson algorithm. From the constellation diagrams displayed in (b), the IQ samples are centered at zero which means the DC offset is removed. The amplitude is also bounded within -600 up to 600, for this particular target, for both I and Q samples which means amplitude imbalance is corrected.

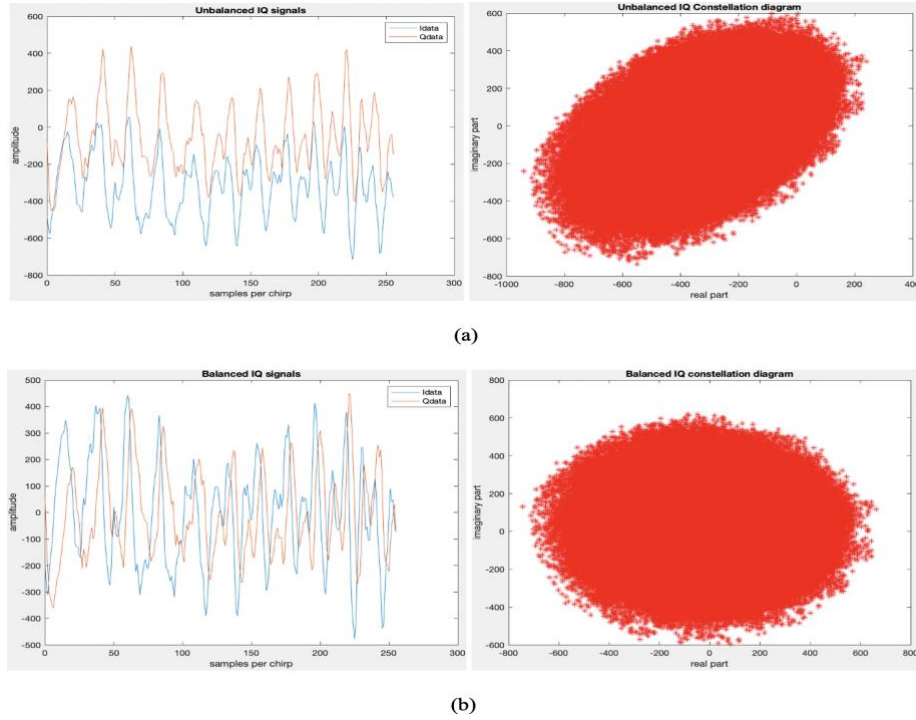


Figure 6: Correcting I-Q Imbalance

### 3.2.2. FFT Algorithm and Estimation of Target Range

After the DC offset and IQ imbalance are corrected, the FFT procedure is performed in a fast time on each row. The frequency spectrum of each row will display peak amplitude at the frequency bins where the target(s) and clutter are located as depicted in Fig. 7. The horn antennas are assumed to be focused on the target; thus, the highest amplitude will represent the target location. Since the FFT procedure resolves objects in range, it is called range-FFT. The output of the range-FFT for a single chirp is shown in Fig. 8.

One of the crucial features of the FMCW radar is its range resolution. This determines the minimum distance between two closely placed objects in which the radar can still segregate the objects. As discussed in chapter one, the range resolution is solely dependent on the bandwidth of the radar. Using equation (6), the range resolution of the radar that was used for collecting the dataset is 4 cm. The chest displacement is assumed to be between 4 mm to 12 mm [30], therefore, the chest displacement takes place within a single range bin. No range bin migration occurs resulting in a single-column range

bin. If the resolution is less than the chest movement, range alignment algorithms such as stated in [31] and [32] have to be implemented to capture the right range bins to model the movement.

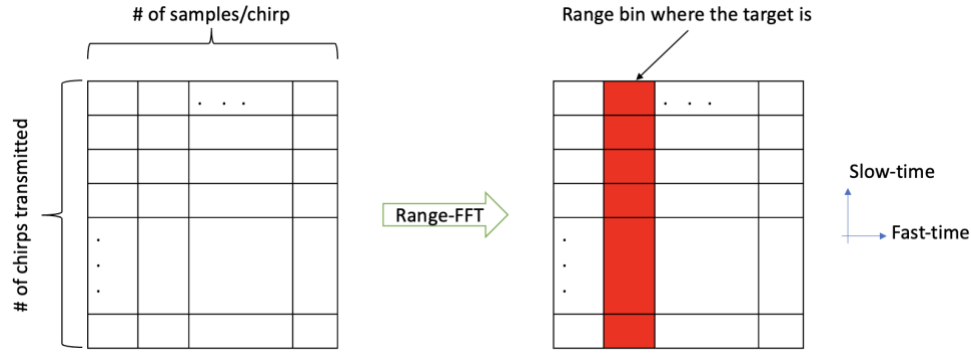


Figure 7: range-FFT operation

Another important feature of radars is the maximum range they can detect. It is already discussed that the range is directly proportional to the IF signal frequency. The maximum intermediate frequency that can be acquired is limited by the sampling rate of the ADC. In other words, the sampling rate of the ADC limits the maximum range of the radar:

$$d_{max} = c * \frac{T_c * f_{IF\_max}}{2B} = \frac{cT_cF_s}{2B} \quad (13)$$

Calculating the max range for the project using the above-derived formula gives 11.002 meters, i.e., the radar can detect targets that are within 11 meters from the antennas. This can be observed from the range-FFT plot in Fig. 8.

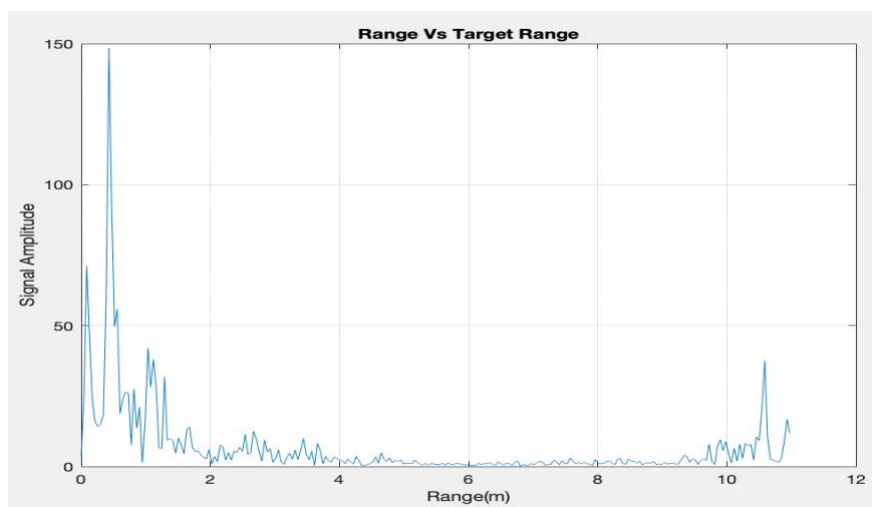


Figure 8: Range-FFT (Range Profile)

After the range-FFT is performed, the target range-bin is found by dividing the target range by the range resolution. Then, the  $n^{\text{th}}$  column that represents the range bin is selected. As mentioned in



section 1.1.2, the range bin represents the chest location. Following the range bin selection, the phase of the column must be extracted to reveal the small displacements of the chest.

### 3.2.3. Phase Extraction, Differential Phase, and Impulse Noise Removal

The classic algorithm for phase demodulation is the arctangent algorithm:  $\phi(t) = \tan^{-1} \left( \frac{Q(t)}{I(t)} \right)$ . However, the drawback of this algorithm is that the result is restricted within  $\left[ -\frac{\pi}{2}, \frac{\pi}{2} \right]$ . If the phase is out of this range, phase wrapping happens. Therefore, an efficient phase unwrapping algorithm is required. Phase unwrapping can be achieved by compensating a  $\pi$  or  $-\pi$  at a transition point. In the presence of amplitude change and noise, unwrapping might induce noise to the phase signal.

Another phase demodulation algorithm is the DACM algorithm. It deploys the derivative of the arctangent function:

$$\frac{d\phi(t)}{dt} = \frac{I(t)Q'(t) - I'(t)Q(t)}{I(t)^2 + Q(t)^2} \quad (14)$$

And the phase can be obtained by integrating the derivative which can discretely be given as:

$$\phi[n] = \sum_{k=2}^n \frac{I[k]\{Q[k] - Q[k-1]\} - \{I[k] - I[k-1]\}Q[k]}{I^2[k] + Q^2[k]} \quad (15)$$

Using DACM algorithm discards the need for a phase unwrapping procedure [25]. Another more efficient algorithm is the modified DACM algorithm. This resembles the DACM algorithm but is not derived from arctan. I and Q signals are modeled as:

$$\begin{aligned} I(t) &= \cos \left[ \frac{4\pi(d_o + \Delta x(t))}{\lambda_c} \right] \\ Q(t) &= \sin \left[ \frac{4\pi(d_o + \Delta x(t))}{\lambda_c} \right] \end{aligned} \quad (16)$$

where  $d_o$  represents the target location and  $\Delta x(t)$  represents the chest displacement. Differentiating both models results into:

$$\begin{aligned} I'(t) &= -\sin \left[ \frac{4\pi(d_o + \Delta x(t))}{\lambda_c} \right] * \frac{4\pi\Delta x'(t)}{\lambda_c}, \\ Q'(t) &= \cos \left[ \frac{4\pi(d_o + \Delta x(t))}{\lambda_c} \right] * \frac{4\pi\Delta x'(t)}{\lambda_c} \end{aligned} \quad (17)$$

And finding  $\Delta x'(t)$  from the above two equations results

$$\Delta x'(t) = \frac{\lambda_c}{4\pi} [I(t)Q'(t) - I'(t)Q(t)] \quad (18)$$

To find  $\Delta x(t)$ , both sides are integrated and discretely can be found by

$$x[n] = \frac{\lambda_c}{4\pi} \sum_{k=2}^n I[k-1]Q[k] - I[k]Q[k-1] \quad (19)$$

and phase can be deduced from  $x[n]$  by using the relationship  $x[n] = \phi[n] \frac{\lambda_c}{4\pi}$ . Extended DACM algorithm decreases the signal-to-noise (SNR) requirement of the signal to be demodulated. This improves the accuracy of the phase demodulation. More details on phase demodulation can be found in [25] and [33]. For this project, extended DACM algorithm was used to extract the phase of the range bin selected in the previous section and Fig. 9 shows the output:

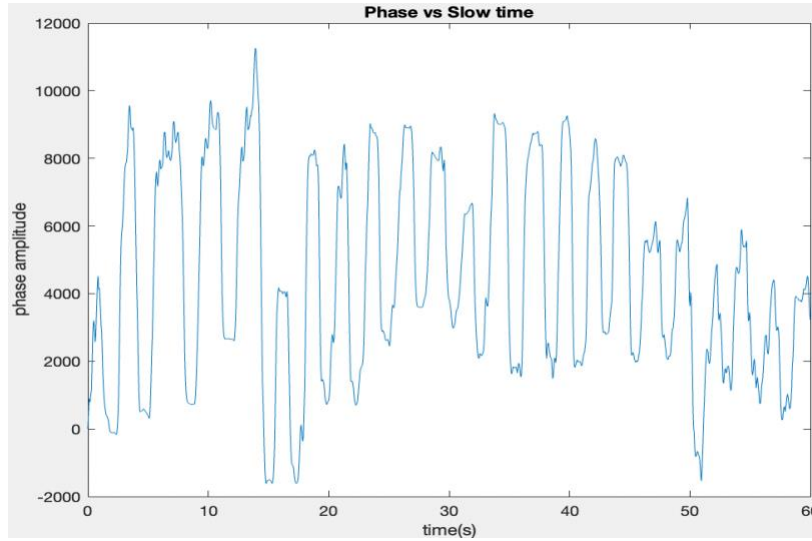


Figure 9: Extracted IF signal Phase

It is easily observed that the extracted phase reveals the sinusoidal-like movement of the chest. The rate of chest movement also represents the breathing rate. The heartbeat signal is more visible on the peaks of the phase signal and hardly noticeable on the sides of the wave. To enhance the heartbeat signal by removing the random body movements and any phase shifts, a differential phase is found by subtracting successive phase values [25]. This operation is followed by impulse noise removal, which corrects any impulse noise corrupted sections that may have been introduced during phase demodulation [27]. This is achieved by computing forward and backward difference for each sample

and if it exceeds a threshold value, it is substituted by an interpolated value. The differential phase before and after impulse noise removal is shown in Fig. 10.

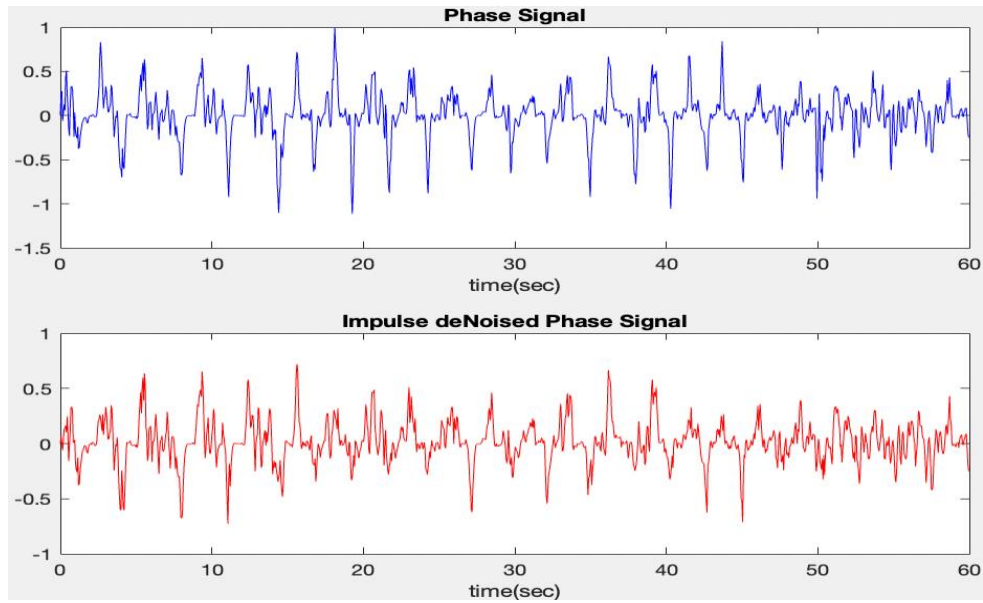


Figure 10: Differential Phase Signal before and after denoising

### 3.2.4. Filtering Based Vital Signs Estimation

The de-noised differential phase signal is then passed through two discrete elliptic bandpass filters with 0.1 Hz - 0.7 Hz and 0.8 Hz - 2.0 Hz cutoff frequencies. The elliptic filter is chosen because the desired ranges are very small thus very sharp transitions are necessary to capture the desired bandwidth. The breathing signal was obtained from the first filter and the heartbeat signal from the latter. The filtered signals can be seen in Fig. 11.

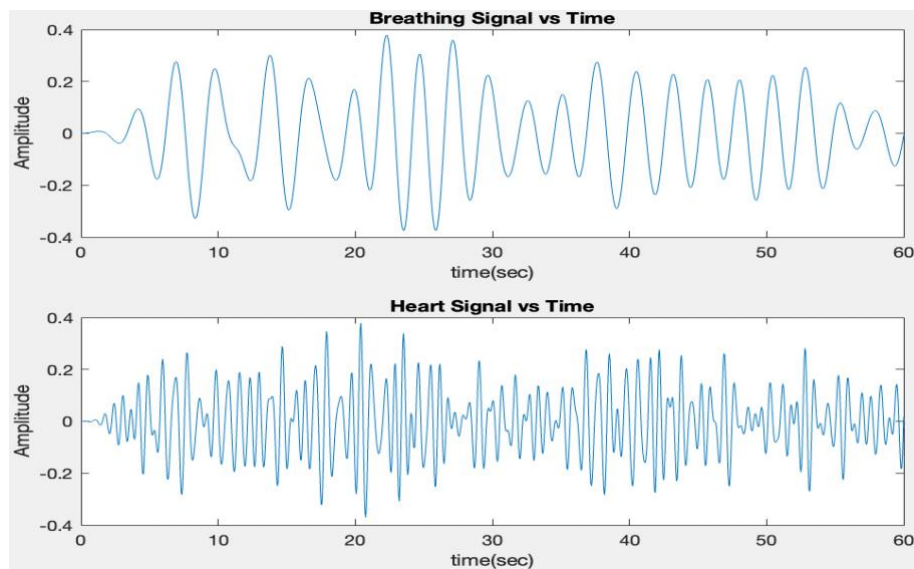


Figure 11: Filter outputs

The breathing rate and heartbeat rates can be estimated by finding the number of peaks of the filter outputs. However, an efficient peak-detecting algorithm such as the one proposed in [34] is required, otherwise, small bumps and transitions i.e., false peaks might be detected and result in wrong estimations. In this project, an autocorrelation algorithm was used to increase the periodicity of the signals and smooth the peaks. Once autocorrelation is performed, the peaks are counted to estimate the breathing and heartbeat rates.

The FFT of the filtered signals comprises a significant amount of noise thus it is not an efficient method to find vital signs, especially the heartbeat rate. The heartbeat signal is corrupted by breathing harmonics and noise of comparable amplitude which makes it difficult to obtain the heartbeat rate in the frequency domain of the filtered signal. Therefore, efficient algorithms that remove the breathing signal harmonics and de-noise the filtered signals are deployed and next is the compressed sensing-based signal reconstruction algorithm.

### 3.2.5. Compressed Sensing Based Signal Reconstruction

Compressed sensing is a technique that employs a signal's sparsity to fully reconstruct the signal from a reduced number of measurements [35]–[37]. The signal's sparsity implies the presence of a few nonzero coefficients in one of its transformation domains. This theory defies the well-known sampling theorem, Nyquist Theorem, which states that a signal must be sampled at least twice the highest frequency present in the signal to ensure full signal reconstruction [35]. [23] notes that breathing and heartbeat signals are proved to be sparse signals in the frequency domain. The idea is to take the filter outputs as available noisy measurements and those samples are used to recover the noiseless vital signs. Both signals are sampled in the frequency domain and then reconstructed using frequency components with high amplitudes. The breathing signal is reconstructed using a single frequency component with the highest amplitude. Since the breathing signal has the highest amplitude in the spectrum, it is easily detected. However, the heartbeat signal was reconstructed using several frequency components of high amplitudes and this is due to the presence of harmonics and noise signals of comparable amplitudes. Therefore, not to mistakenly pick a wrong frequency component, several components are used to reconstruct the signal.

$$y = Ax \tag{20}$$

The linear transformation shown in equation (20) is used to model compressed sensing.  $y$  represents the available measurements,  $x$  represents the sparse signal, and  $A$  represents the transformation basis.  $A$  is composed of a sensing basis and a representation basis. Since the signals are being sampled in the frequency domain, the Fourier transform representation basis is used. And sensing basis represents the domain from which a smaller amount of data is obtained from the signal.  $y$  is a  $K \times 1$

matrix,  $A$  is a  $K \times N$  matrix, and  $x$  is a  $N \times 1$  matrix.  $A$  is a fat matrix which means the above-stated model is underdetermined. The equation can then be solved using a convex algorithm or greedy pursuit algorithms subjected to either of the following two constraints: i) to result in the least error with a pre-known number of sparse coefficients of  $x$ , or ii) to result in the sparsest  $x$  given a boundary error. In this project, the first approach is opted. For the breathing signal, one coefficient was assumed which results in the breathing signal reconstruction using the frequency component with the highest amplitude, whereas as mentioned before, a few coefficients were assumed for the heart signal. For reconstructing the signal, the fundamental minimization problem can be written as:

$$\min ||x||_0 \quad \text{subject to} \quad y = Ax \quad (21)$$

The  $l_0$ - norm is not a convenient method for minimization problems. However, greedy algorithms known as matching pursuit algorithms can be used to find the best approximation if the number of non-sparse coefficients can be estimated. For this project, an improved greedy algorithm known as orthogonal matching pursuit (OMP) which is explained in [36], and [37] is used. The outcomes of this algorithm for breathing signal and heartbeat signal reconstruction are shown in Fig. 12 and Fig. 13 respectively.

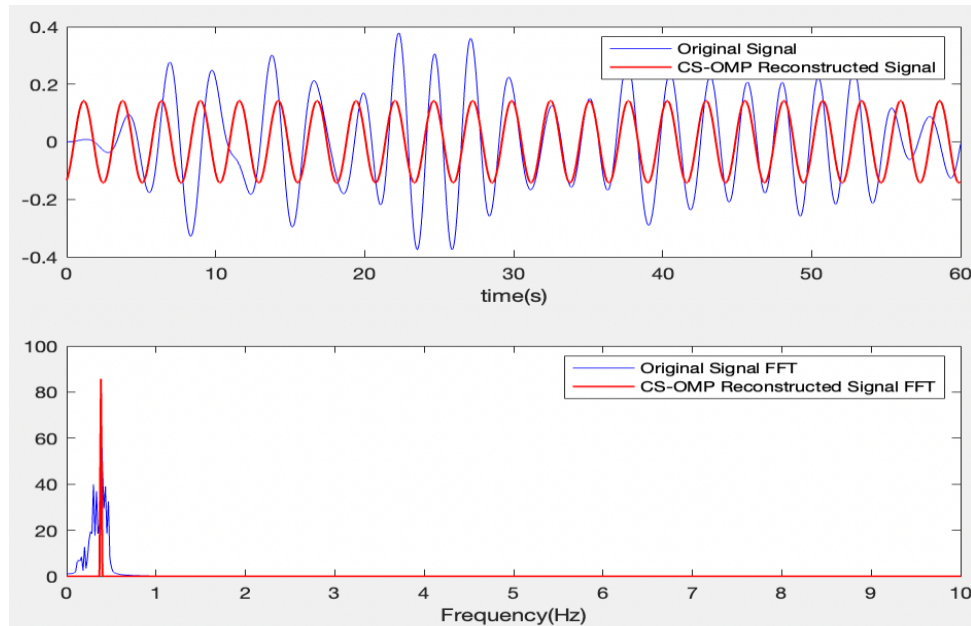


Figure 12: CS-OMP Reconstructed Breathing Signal

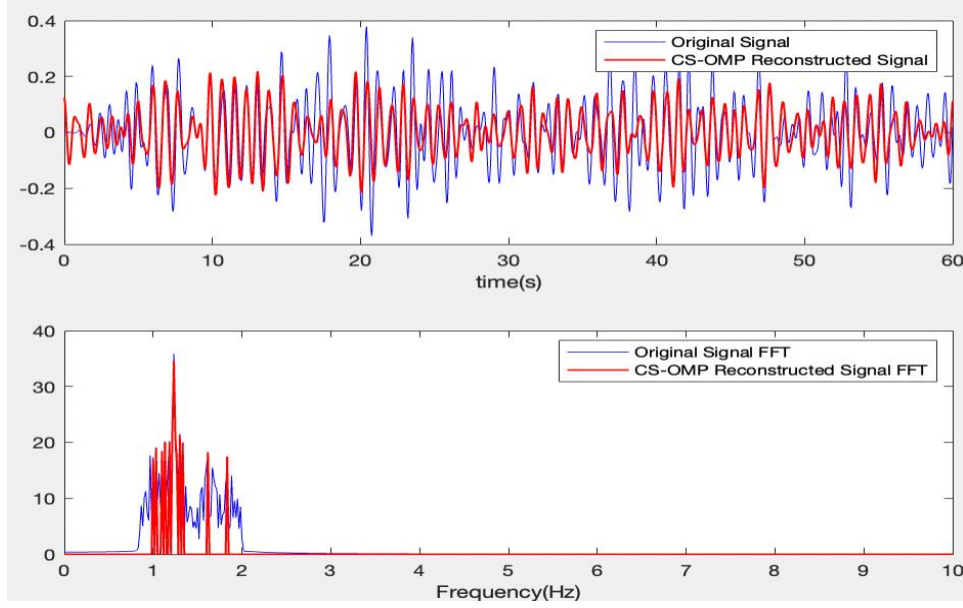


Figure 13: CS-OMP Reconstructed Heartbeat Signal

After obtaining the FFT of the reconstructed signal, the peak frequency is used to estimate the vital signs. The breathing rate is estimated perfectly. And for heartbeat rate estimation, the breathing signal harmonics were removed followed by peak detection. Moreover, autocorrelation was performed on the reconstructed signals to obtain the vital signs in the time domain. For further detailed visualization of the frequency components of the differential phase signal, wavelet decomposition was implemented.

### 3.2.6. Wavelet Decomposition

The Fourier transform is useful in analyzing the frequency components of stationary signals. However, performing Fourier analysis on signals that are non-stationary results in frequency components without any regard to the time of occurrence. Wavelet transform results in analyzing signals into different frequencies at different resolutions known as multiresolution analysis [38], [39]. This is achieved by using new basis functions called wavelets which act as scalable window functions. The general formula for wavelet transform is:

$$F(\tau, s) = \frac{1}{\sqrt{|s|}} \int_{-\infty}^{+\infty} f(t) \psi^* \left( \frac{t - \tau}{s} \right) d(t) \quad (22)$$

$\psi(t)$  is the wavelet function and its width can be changed by changing the value of scale parameter  $s$ . Expanded wavelets resolve low-frequency components while shrunk wavelets are good for resolving high-frequency components. Wavelet transform can also be equated to a series of filters [39]. Each decomposition level is composed of a low-pass filter and a high-pass filter. In the first decomposition

level, the input signal is broken down into two signals each with approximately half the original bandwidth. In the next level, the signal from the low-pass filter is then again broken down into two signals each with approximately half its bandwidth and this goes on for the rest of the levels. This can be demonstrated in Fig. 14.

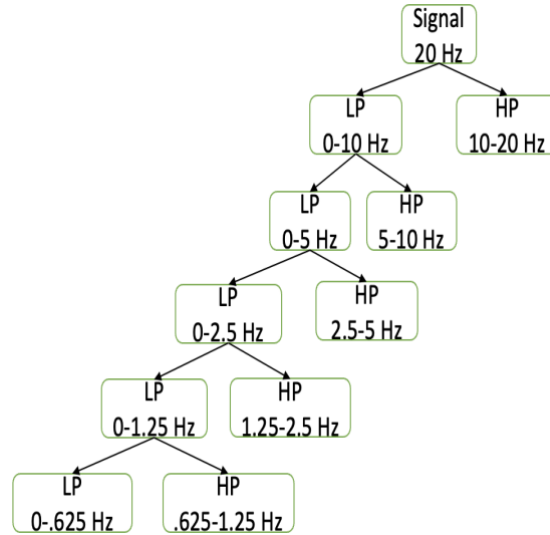


Figure 14: Filtering property of the Wavelet Decomposition

Figure 15 shows the decomposition of the differential phase in the time and frequency domain. The signal was decomposed into five levels using Daubechies 5 ('db5') wavelet. Wavelet de-noising was also performed to remove noise components after decomposition. Figure 15 shows a detailed time and frequency characteristics of the vital signs. The frequency domain briefly shows the frequency components at different decomposition levels of the signal.

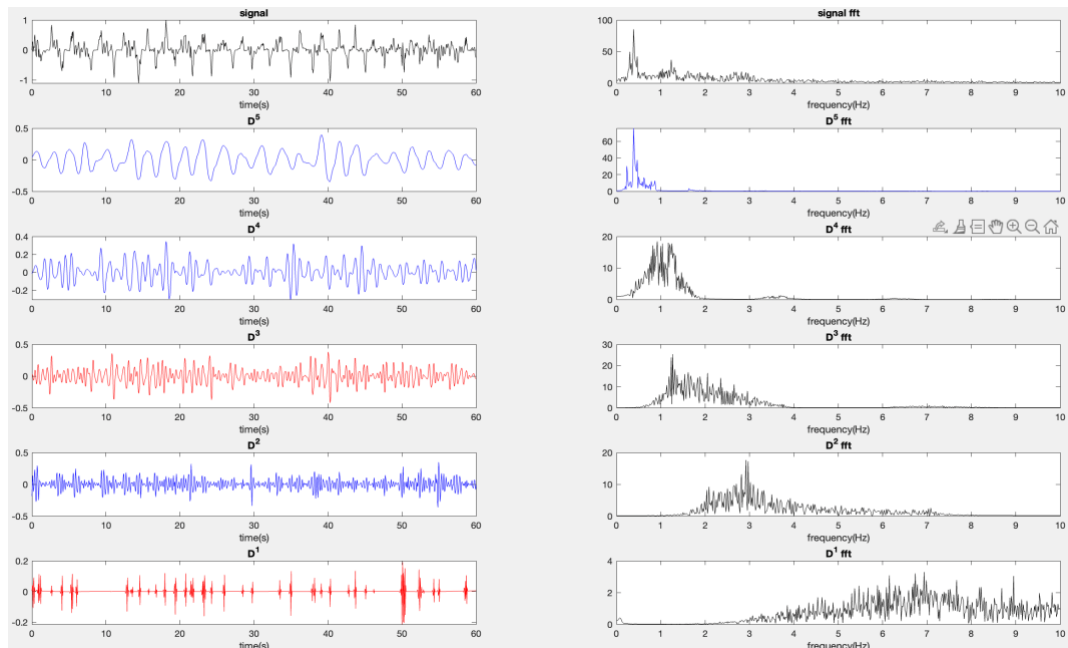


Figure 15: Wavelet Decomposition Output

It can be observed that the heartbeat signal is extracted in the third level decomposition and the breathing signal in the fifth level decomposition. Before heartbeat rate estimation using peak detection, the breathing signal harmonics are removed.

### 3.3. Performance Analysis

The performance of the above-explained chain of algorithms was compared with the measurements that were obtained from a clinically approved vital signs monitoring sensor, Nihon Kohden. The sensor was used as a reference during dataset collection from the children. As mentioned before, the dataset of the four children aged between 9 and 13 years was used to analyze the performance of the algorithm. To avoid large movement corrupted data, a dataset accumulated between 20 and 60 seconds was used. The Nihon Kohden sensor measures the vital rates per second. Therefore, for comparison the average values of the measurements accumulated between 20 and 60 seconds are used. The datasets from Nihon Kohden and the algorithm measurements are listed in Table 2. In the time domain, the vital signs per minute are calculated by detecting and counting the peaks and using the following equation:

$$Rate = peaks\ detected * \frac{60\ secs/min}{time\ range\ of\ measurement\ in\ sec} \quad (23)$$

In the frequency domain, the highest peak,  $f_{peak}$ , in the frequency range of interest was detected and the rate per minute was calculated using:

$$Rate = f_{peak} * \frac{60\ sec}{min} \quad (24)$$

Table 2: Breathing rate and Heartbeat rate estimations

Methods	Nihon Kohden		Filtering		Compressed Sensing				Wavelet Decomposition	
	BR	HR	BR	HR	BR		HR		BR	HR
			autocorr	autocorr	autocorr	FFT	autocorr	FFT	FFT	FFT
i. Child11	29.93	90.33	27.75	95	29.25	28.5	87.75	90	30	87
ii. Child14	20.4	76.4	18.75	78.50	20.25	19.5	77.25	76.5	24	76.5
iii. Child35	20	85.2	18.75	93.75	18.75	18	89.25	85.5	18	85.5
iv. Child49	23	82.75	23.25	83.25	24.75	24	79	78	24	78



As shown in Table 2, the used algorithms result in satisfactory results compared to the reference sensor. Generally, all the algorithms estimated the breathing rate of the subjects satisfactorily with a maximum of three breaths offset. In the time domain, compressed sensing-based signal reconstruction resulted in better estimations compared with filtering as expected. For heart rate estimation, the compressed sensing-based signal reconstruction resulted in the most accurate estimations in the frequency domain. Whereas time domain estimation using the filtering algorithm resulted in the most deviated rates. Wavelet decomposition also resulted in almost similar results as the compressed sensing in FFT.

Although the algorithm resulted in satisfactory estimations, the subjects were only 4. The algorithm was designed for adults and did not consider large body movements. And due to the lack of an adult dataset recorded by FMCW radar on the internet, a children's dataset was used. Therefore, for better performance analysis, the algorithms have to be validated using adult dataset in the future.

# Chapter 4: Hardware Radar IC Measurement

## 4.1. Measuring the Tx and Rx Antennas

### 4.1.1. Measuring the Receiver: Transmitter Block

The transmitter block was set up using a signal generator, an R&D®SMZ170 multiplier, and an antenna. The specs for the multiplier can be found in [40]. The signal generator generated a signal of 13.1999 GHz frequency with 8.5 dBm power which is the input power requirement of the multiplier. The signal is then fed to the multiplier which has a 170/14.2 multiplication factor. The connections and device arrangements can be seen in Fig. 16. The phase noise of the transmitted signal was also measured and can be shown in Fig. 17. The noise within the phase-locked loop (PLL) bandwidth can be seen to be stabilized due to the feedback control mechanism design. The output signal of a 158 GHz frequency is then directed to the horn antenna which faces toward the receiver horn antenna.

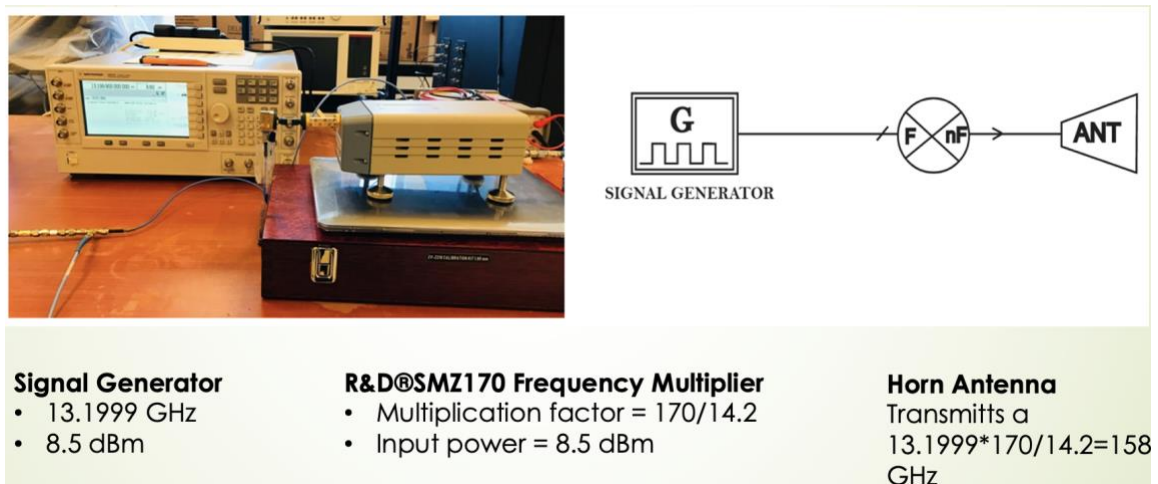


Figure 16: Transmitter Setup

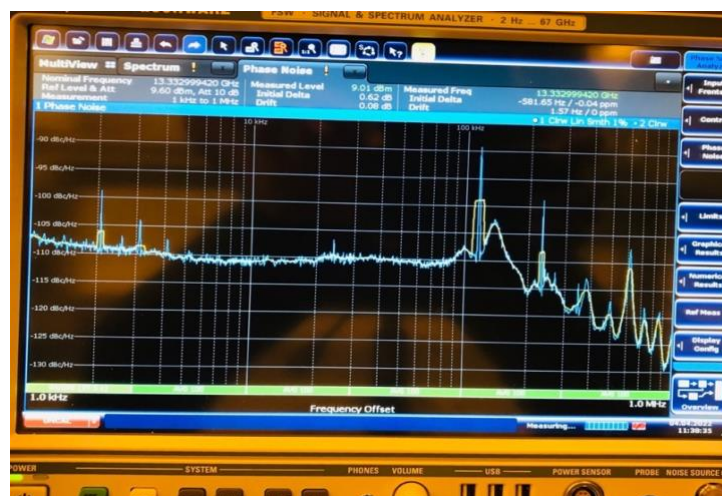


Figure 17: Transmitted Signal Phase Noise

### 4.1.2. Measuring the Transmitter: Receiver Block

The transmitted signal is received by an identical horn antenna that is attached to a WHMB-06-0001 harmonic mixer with a gain of 170/14.17 [41]. The mixer does not possess an integrated local oscillator (LO)/intermediate frequency (IF) diplexer and only has two ports. One of the ports is connected to the antenna and the second port takes the LO input and outputs LO and IF signals. To segregate the input and output of the mixer, a combiner with three ports was used. The setup diagram is shown in Fig. 18.

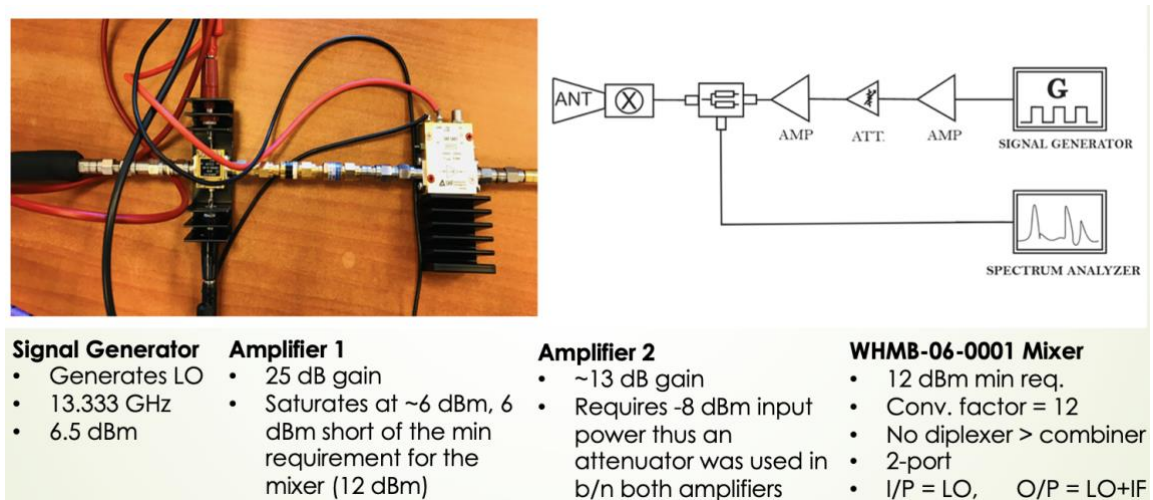


Figure 18: Receiver Setup

A 13.333 GHz LO was generated using a second signal generator. The main challenge faced was satisfying the 12 dBm input power requirement of the mixer. The combiner further attenuates the generated LO. Therefore, an amplifier with a 25 dB gain was used to amplify the signal generated. Although the gain of the amplifier was theoretically enough, the amplifier saturated approximately at 6 dBm. A second amplifier with 13 dB gain was then added. The amplifier with the smallest saturation point i.e., the one with 25 dBm gain was connected near the signal generator followed by the second amplifier. However, the second amplifier required -8 dBm input power thus an attenuator was used to attenuate the output of the first amplifier. The generated LO was then tuned to meet the input requirements of the amplifier and was finally set to 6.5 dBm. This LO is then directed to the mixer and the desired LO+IF is acquired using the combiner. The IF can then be acquired using a lowpass filter or a bandpass filter. The IF signal was captured at 1.6 GHz with -44 dBm as shown in Fig. 19.

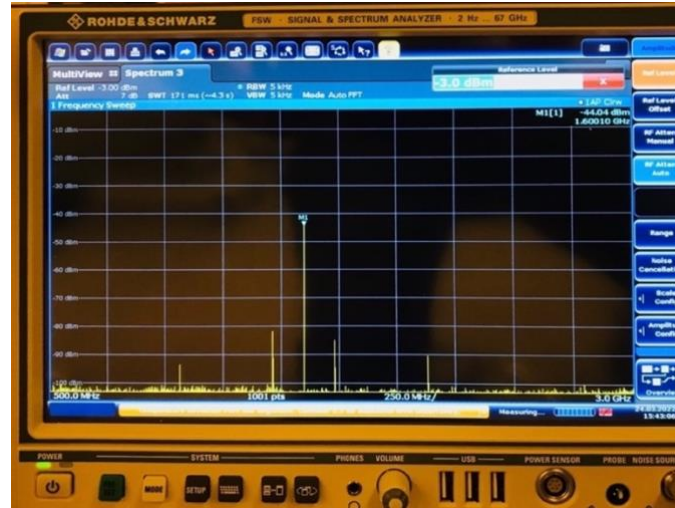


Figure 19: Acquired IF Signal

### 4.1.3. Biasing the IC

Almost half of the bias sources of the radar IC are current sources. Thus, external resistors were used to draw the required current from voltage sources shown in Fig. 20.



Figure 20: Radar IC Biasing Circuitry

Of the 12 printed circuit boards (PCBs), only one was successfully biased. Most of the PCBs failed to draw the current that was required to bias some of the components. The main components that failed to draw the needed current are the power amplifier (PA) and low-noise amplifier (LNA). The problem might be from the fabrication process of the chips or faults during bonding. The issue is not from the design because few PAs and LNAs were able to draw the needed current. The PCB that was biased successfully was experimented with at different frequencies to obtain the IF signal, but it was not successful. Therefore, the hardware measurement could not continue beyond that.



## 4.2. ADC and ADS9-V2EBZ Evaluation Board

The I-Q signals from the mixer are directed to an ADC to be digitized and then later processed by the evaluation board. A high-speed 16-bit ADC evaluation board with capabilities of 6 gbps called AD9082-FMCA-EBZ is to be used in the final project. The I-Q signals are captured using AD9082 and are directed to the ADS9-V2EBZ board via FMC connector. The ADS9-V2EBZ board is equipped with an embedded MicroZed board which is used to program the Kintex Ultrascale+ FPGA which is integrated into the board as well. Moreover, application software from Analog Devices called Analysis, Control, and Evaluation (ACE) is used to upload the FPGA image, configure the devices, and capture the ADC sampled data for analysis. Fig. 21 shows the setup for the ADC and the evaluation board. Moreover, more details on the connections and setup configurations can be found in [42].

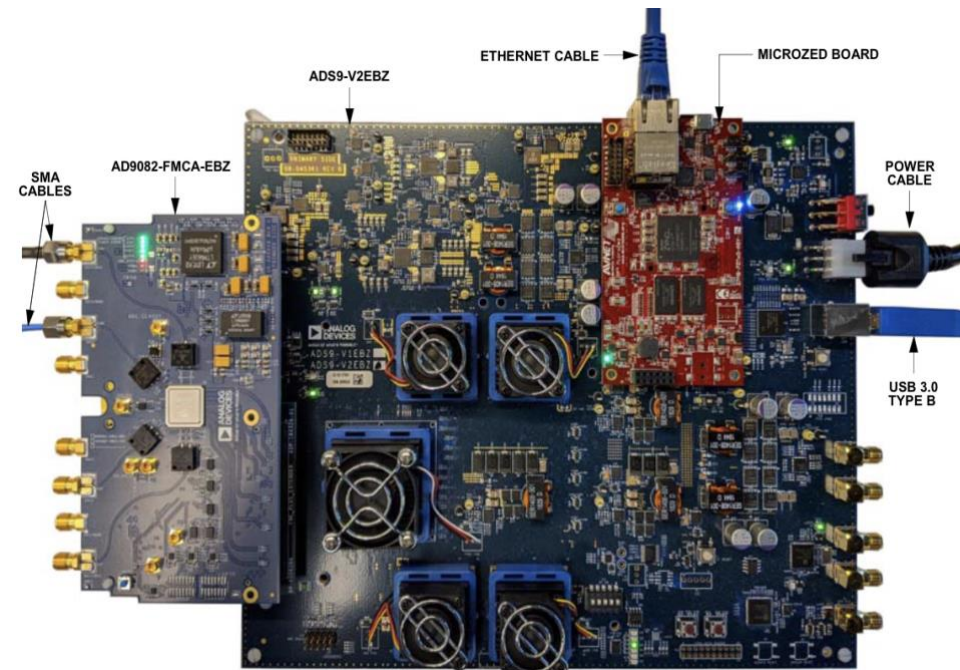


Figure 21: ADC and the Evaluation Board Setup

The AD9082 with ADS9 evaluation board can be configured and programmed using an application programming interface (API). Once the signal is captured using the above setup, MATLAB is used to process the Data. The MATLAB API files were provided by Analog Devices Inc. The following details the steps and codes that were used to configure and set communication between MATLAB and the boards [43].

- 1) MicroZed Connection Setup: a memory card is installed on the MicroZed board and is configured to connect to the host computer where MATLAB is running.
- 2) FPGA image should be configured using ACE software and the AD9082 and FPGA are linked. Otherwise, chip-to-chip bridge error will occur.
- 3) Some files that are provided by Analog Devices are copied onto the MicroZed. Those include:
  - i) Standalone app – is a Linux application that contains files to configure the AD9082 device on the ADS9 platform.

- ii) Xtras app – is a Linux application for loading vectors and capturing data on the ADS9 platform.
- 4) Those files listed above are copied into the MicroZed memory and their functionalities are checked.

The file applications that are copied to the MicroZed board are to be remotely run using MATLAB. MATLAB uses the built-in system function to use the terminal shell and connect and remotely control the applications. Furthermore, editable bash shell scripts are provided that connect, configure, call, copy, and run those applications from/to MATLAB. Those scripts are:

- i) txte\_app\_run.sh: - remotely execute the standalone app.
- ii) xtra\_app\_run\_tx.sh: - remotely executes the Xtras app for creating and downloading vectors. This won't be used in the final project unless ADC files are first to be saved and later fed to the ADS9 platform.
- iii) Xtras\_app\_run\_rx.sh: - remotely execute the Xtras app for capturing data. Captured files are copied to the host computer.

To verify the communication between MATLAB and the boards, 10 MHz single-tone IQ signals are generated using MATLAB. The data are saved in a file and are copied to the MicroZed microSD card remotely using the xtra\_app\_run\_tx.sh script. This data is then directed via the digital to analog converters (DACs) and is looped back to the ADCs. The setup is shown below:

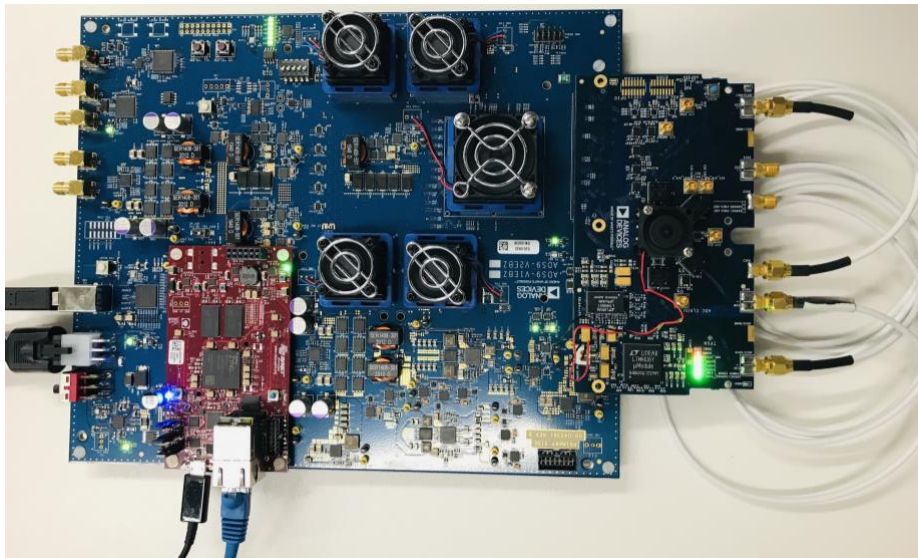
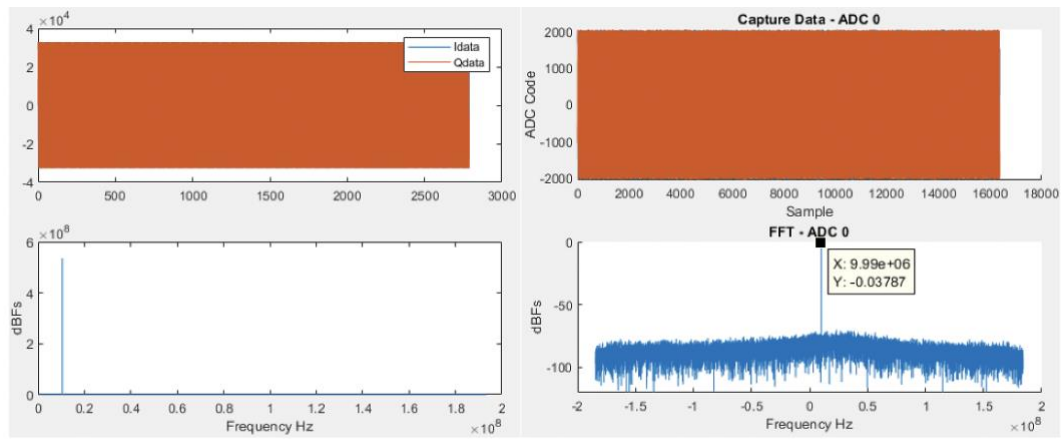


*Figure 22: ADC and Evaluation Board Setup Test Configuration*

The ADC captures the data provided and the output is saved in files which are then transferred to the host computer to be processed using MATLAB. The transmitted and ADC-captured data are shown in Fig. 23.



(a)

(b)

Figure 23: Transmitted and Captured Data

# Chapter 5: Conclusion and Future Work

## 5.1. Conclusion

In this thesis project, vital signs detection using FMCW radar has been presented. The basic theoretical and mathematical working principles of FMCW radar and its superiority over other radar types were explained. The frequency and phase of the IF signal depend on the range of the target. In chapter 3, an algorithm that takes advantage of the IF signal frequency and phase to locate a target and model the chest movement was introduced. Before extracting the IF signal frequency and phase, the algorithm addresses DC offset and IQ imbalances that are introduced from the hardware. Then, the target location was detected and evaluated using the FFT algorithm. Based on the target location, the desired range bin that represents the chest was selected. Modified DACM algorithm was then used to extract the phase of the range bin of interest and the demodulated phase models the sinusoidal movement of the chest. Filtering, compressed sensing-based signal reconstruction, and wavelet decomposition were then used to detect the vital signs and estimate the vital rates. For time domain estimations, autocorrelation was performed to increase the periodicity of the vital signals before peak detection. And for frequency domain estimations, breathing harmonics were removed before heartbeat signal detection.

The rate estimations were compared to a dataset that was accumulated using Nihon Kohden vital signs monitoring device. The algorithm was first developed assuming still adult subjects. It did not put the large movement of the target into consideration. Due to the lack of a public adult dataset, a dataset of children was used. Since the children were young and tend to move, the dataset of 4 children who are of age 9 up to 13 was used. The algorithms satisfactorily estimated the vital rates of the targets and are expected to perform better on an adult dataset.

In chapter 4, this research also presented a yet-to-be-finalized measurement procedure on a vital sign monitoring radar IC chip that operates at 160 GHz frequency. The measurement was halted due to failure to successfully bias the available bonded chips. However, antenna measurement procedures were implemented. The AD9082 ADC and the ADS9 evaluation board that are to be used to capture and quantize the IF signal from the radar IC are also investigated. API usage and scripts that are used for remote configuration and capturing data are also discussed. In the end, the connection and scripts were successfully tested by looping back a signal generated in MATLAB via the DACs and capturing it using the ADCs.



## 5.2. Future Work

Even though the vital rates were successfully acquired, several improvements can be added to the algorithms. For instance, random small body movements are dealt with phase differentiation, but large and continuous body movements can be detected and corrected or removed by adding gain control algorithms. Moreover, the decomposition levels where the breathing signal and heartbeat signal are detected during wavelet decomposition can also be used to extract the vital signs in the time domain.

The code was developed for adults, and it is expected to perform better on the adult dataset because adults' chest movement is higher compared to children's thus the heartbeat amplitude would be more detectable. In the future, the radar IC chip being measured will be used to obtain datasets in a more controlled environment and the dataset will be used on the algorithm explained. The AD9082 and ADS9-V2EBZ boards will also be used to capture the IF data and as a means of communication between the radar IC and the host computer with MATLAB.

Moreover, the ADS9 evaluation board has an integrated FPGA thus the MATLAB code that has been developed can be translated into a hardware description language (HDL) and be used to program the FPGA. This would enable the FPGA to be the standalone signal processing center and eliminate the use of a host computer.

# Bibliography

- [1] C. Gu, "Short-range noncontact sensors for healthcare and other emerging applications: A review," *Sensors (Switzerland)*, vol. 16, no. 8. MDPI AG, Aug. 01, 2016. doi: 10.3390/s16081169.
- [2] V. Milovanovic, "On fundamental operating principles and range-doppler estimation in monolithic frequency-modulated continuous-wave radar sensors," *Facta universitatis - series: Electronics and Energetics*, vol. 31, no. 4, pp. 547–570, 2018, doi: 10.2298/fuee1804547m.
- [3] D. Wang, S. Yoo, and S. H. Cho, "Experimental comparison of ir-uwband radar and fmcw radar for vital signs," *Sensors (Switzerland)*, vol. 20, no. 22, pp. 1–22, Nov. 2020, doi: 10.3390/s20226695.
- [4] G. Wang, J. M. Munoz-Ferreras, C. Gu, C. Li, and R. Gomez-Garcia, "Application of linear-frequency-modulated continuous-wave (LFMCW) radars for tracking of vital signs," *IEEE Trans Microw Theory Tech*, vol. 62, no. 6, pp. 1387–1399, 2014, doi: 10.1109/TMTT.2014.2320464.
- [5] Tariq, Abubakar, and H. G. Shiraz. "Doppler radar vital signs monitoring using wavelet transform." In *2010 Loughborough Antennas & Propagation Conference*, pp. 293-296. IEEE, 2010
- [6] M. Alizadeh, G. Shaker, J. C. M. de Almeida, P. P. Morita, and S. Safavi-Naeini, "Remote monitoring of human vital signs using mm-Wave FMCW Radar," *IEEE Access*, vol. 7, pp. 54958–54968, 2019, doi: 10.1109/ACCESS.2019.2912956.
- [7] M. Mercuri, I. R. Lorato, Y. H. Liu, F. Wieringa, C. van Hoof, and T. Torfs, "Vital-sign monitoring and spatial tracking of multiple people using a contactless radar-based sensor," *Nat Electron*, vol. 2, no. 6, pp. 252–262, Jun. 2019, doi: 10.1038/s41928-019-0258-6.
- [8] M. Alizadeh, "FMCW Radar System," 2019.
- [9] Rao, Sandeep. "Introduction to mmWave sensing: FMCW radars." *Texas Instruments (TI) mmWave Training Series* (2017): 1-11
- [10] I. Seflek, Y. E. Acar, and E. Yaldiz, "Small motion detection and non-contact vital signs monitoring with continuous wave doppler radars," *Elektronika ir Elektrotechnika*, vol. 26, no. 3, pp. 54–60, Jun. 2020, doi: 10.5755/j01.eie.26.3.25810.
- [11] L. Stingeni *et al.*, "The role of acrylic acid impurity as a sensitizing component in electrocardiogram electrodes," *Contact Dermatitis*, vol. 73, no. 1, pp. 44–48, Jul. 2015, doi: 10.1111/cod.12357.
- [12] A. Ahmad, J. C. Roh, D. Wang, and A. Dubey, *Vital Signs Monitoring of Multiple People using a FWCW Millimeter-Wave Sensor*. IEEE, 2018.
- [13] S. Iyer *et al.*, "mm-Wave Radar-Based Vital Signs Monitoring and Arrhythmia Detection Using Machine Learning," *Sensors*, vol. 22, no. 9, May 2022, doi: 10.3390/s22093106.
- [14] B. Zhang *et al.*, "A Framework for Remote Interaction and Management of Home Care Elderly Adults," *IEEE Sens J*, vol. 22, no. 11, pp. 11034–11044, Jun. 2022, doi: 10.1109/JSEN.2022.3170295.

- [15] M. Kebe, R. Gadhafi, B. Mohammad, M. Sanduleanu, H. Saleh, and M. Al-qutayri, "Human vital signs detection methods and potential using radars: A review," *Sensors (Switzerland)*, vol. 20, no. 5. MDPI AG, Mar. 01, 2020. doi: 10.3390/s20051454.
- [16] Razavi, Behzad. *Design of analog CMOS integrated circuits*. 清华大学出版社有限公司, 2005
- [17] S. Yoo *et al.*, "Radar recorded child vital sign public dataset and deep learning-based age group classification framework for vehicular application," *Sensors*, vol. 21, no. 7, Apr. 2021, doi: 10.3390/s21072412.
- [18] G. Paterniani, D. Sgreccia, A. DAVOLI, G. Guerzoni, P. di Viesti, and A. C. Valenti, "Radar-based Monitoring of Vital Signs: A Tutorial Overview", doi: 10.36227/techrxiv.19212918.v1.
- [19] W. Lv, W. He, X. Lin, and J. Miao, "Non-contact monitoring of human vital signs using fmcw millimeter wave radar in the 120 ghz band," *Sensors*, vol. 21, no. 8, Apr. 2021, doi: 10.3390/s21082732.
- [20] Y. Hu, Z. Xia, and F. Xu, "Using FMCW Millimeter-Wave Radar to Realize the Detection of Vital Signs," in *2021 International Conference on Microwave and Millimeter Wave Technology, ICMMT 2021 - Proceedings*, 2021. doi: 10.1109/ICMMT52847.2021.9617873.
- [21] T.-Y. J. Kao and J. Lin, "Vital Sign Detection Using 60-GHz Doppler Radar System."
- [22] S. Wang *et al.*, "A novel ultra-wideband 80 GHz FMCW Radar System for contactless monitoring of Vital Signs."
- [23] Y. Wang, W. Wang, M. Zhou, A. Ren, and Z. Tian, "Remote monitoring of human vital signs based on 77-GHZ MM-WAVE FMCW radar," *Sensors (Switzerland)*, vol. 20, no. 10, May 2020, doi: 10.3390/s20102999.
- [24] "Driver Vital Signs-Developer's Guide.", *Texas Instruments (TI) mmWave Labs*, [Online], Available: [https://github.com/bigheadG/mmWaveDocs/blob/master/DriverVitalSigns\\_DevelopersGuide.pdf](https://github.com/bigheadG/mmWaveDocs/blob/master/DriverVitalSigns_DevelopersGuide.pdf)
- [25] K. Han and S. Hong, "Differential phase doppler radar with collocated multiple receivers for noncontact vital signal detection," *IEEE Trans Microw Theory Tech*, vol. 67, no. 3, pp. 1233–1243, Mar. 2019, doi: 10.1109/TMTT.2018.2884406.
- [26] S. Ma, W. Xue, K. Chen, and Z. Wang, "Radar Vital Signs Detection Method Based on Variational Mode Decomposition and Wavelet Transform," in *Proceeding - 2021 China Automation Congress, CAC 2021*, 2021, pp. 7469–7474. doi: 10.1109/CAC53003.2021.9728129.
- [27] M. Xiang, W. Ren, W. Li, Z. Xue, and X. Jiang, "High-Precision Vital Signs Monitoring Method Using a FMCW Millimeter-Wave Sensor," *Sensors*, vol. 2022, p. 7543, 2022, doi: 10.3390/s22197543.
- [28] L. Ren, "Noncontact Vital Signs Detection," 2017. [Online]. Available: [https://trace.tennessee.edu/utk\\_graddiss](https://trace.tennessee.edu/utk_graddiss)
- [29] S. W. Ellingson, "Correcting I-Q Imbalance in Direct Conversion Receivers," 2003.

- [30] A. Singh, S. U. Rehman, S. Yongchareon, and P. H. J. Chong, "Modelling of chest wall motion for cardiorespiratory activity for radar-based NCVS systems," *Sensors (Switzerland)*, vol. 20, no. 18. MDPI AG, pp. 1–13, Sep. 02, 2020. doi: 10.3390/s20185094.
- [31] Wang, Junfeng, and Xingzhao Liu. "Improved global range alignment for ISAR." *IEEE Transactions on Aerospace and Electronic Systems* 43, no. 3 (2007): 1070-1075.
- [32] T. \_ S. Sauer, "[IEEE Transactions on Aerospace and Electronic Systems 1995-jul vol. 31 iss. 3] Sauer, T.\_ Schroth, A. - Robust range alignment algorithm via Hough transform in an ISAR imaging system (1995) [10.1109\_7.395222] - libgen.li".
- [33] J. P. Havlicek, A. C. Bovik, J. Liu, and C. Gu, "Demodulation Algorithm AM-FM Image Models: Fundamental Techniques and Emerging Trends Radar-based vital signs monitoring 9.2.1.2 Phase demodulation algorithm."
- [34] J. Y. Kim, J. H. Park, S. Y. Jang, and J. R. Yang, "Peak detection algorithm for vital sign detection using doppler radar sensors," *Sensors (Switzerland)*, vol. 19, no. 7, Apr. 2019, doi: 10.3390/s19071575.
- [35] E. J. Candes and M. B. Wakin, "An introduction to compressive sampling: A sensing/sampling paradigm that goes against the common knowledge in data acquisition," *IEEE Signal Process Mag*, vol. 25, no. 2, pp. 21–30, 2008, doi: 10.1109/MSP.2007.914731.
- [36] L. Stanković, E. Sejdić, S. Stanković, M. Daković, and I. Orović, "A Tutorial on Sparse Signal Reconstruction and Its Applications in Signal Processing," *Circuits Syst Signal Process*, vol. 38, no. 3, pp. 1206–1263, Mar. 2019, doi: 10.1007/s00034-018-0909-2.
- [37] V. Ravuri, S. K. Terlapu, and S. S. Nayak, "Performance evaluation of compressive sensing matching pursuit backtracking iterative hard thresholding algorithm for improving reconstruction," *Journal of Intelligent and Fuzzy Systems*, vol. 40, no. 4, pp. 5777–5786, 2021, doi: 10.3233/JIFS-189417.
- [38] C. H. Choi, J. H. Park, H. N. Lee, and J. R. Yang, "Heartbeat detection using a Doppler radar sensor based on the scaling function of wavelet transform," *Microw Opt Technol Lett*, vol. 61, no. 7, pp. 1792–1796, Jul. 2019, doi: 10.1002/mop.31823.
- [39] Chun-Lin, Liu. "A tutorial of the wavelet transform." *NTUEE, Taiwan* 21 (2010): 22
- [40] Rohde and Schwarz (2013), "R&S®SMZ Frequency Multiplier Specifications,"
- [41] "WR-06 Harmonic Mixer 110- 170 GHz: WHMB-06-0001" [Online]. Available: <https://farran.com/wp-content/uploads/2022/06/WHMB-06-0001.pdf>
- [42] Analog Devices Inc. (2021), "AD9081/AD9082/AD9986/AD9988 User Guide", Norwood, MA 02062-9106, USA
- [43] Analog Devices Inc. (2021), "TxFE/MxFE Eval App Extras-User Guide."

# Appendices

## Appendix A: Algorithm Codes

### i. S.W. Ellingson Algorithm

```
function [ldata__,qdata__] = SWEllingson_(ldata, qdata)

Inorm = max(ldata);
Qnorm = max(qdata);

ldata = ldata/Inorm;
qdata = qdata/Qnorm;

lmean = mean(ldata);
qmean = mean(qdata);

ldata_ = ldata - lmean;
qdata_ = qdata - qmean;

alpha = sqrt(2 * mean(ldata_*ldata_));

sin_ = 2/alpha * (mean(ldata_*qdata_));

cos_ = sqrt(1-(sin_)^2);

A_ = 1/alpha;
C_ = -sin_/(alpha*cos_);
D_ = 1/cos_;

ldata__ = Inorm * (A_ * ldata_);
qdata__ = Qnorm * (C_ * ldata_ + D_ * qdata_);

end
```

### ii. Range – FFT Algorithm

```
function [rangeProfile_fft, peakAmp, maxFreq] = rangeFFT (ldata, qdata, param)

cplx = zeros(param.numChirps,param.numSamplesperChirp);
X = zeros(param.numChirps, param.numSamplesperChirp);
Y = zeros(param.numChirps, param.numSamplesperChirp);

%% fasttime FFT operation
```

```

for i=1:param.numChirps

    cplx(i,:) = complex(Idata(i,:), Qdata(i,:));
    N = length(cplx(i,:));
    X(i,:) = fft(hanning(1,N).*cplx(i,:))/N;
    fx = (0:N-1)*param.adcSamplingrate/N;
    Y(i,:) = fftshift(X(i,:));
    fy = (-N/2:N/2-1)*param.adcSamplingrate/N;
    [peakAmp{i}, maxFreq{i}] = findpeaks((abs(X(i,:))),fx);

end

rangeProfile_fft = X;

end

```

### iii. Peak Frequency Detection

```

function [peakFreq] = maxFreq(peakAmplitudes, peakFrequencies)

len_peak = length(peakAmplitudes);
len_freq = length(peakFrequencies);
peakAmp = zeros(1,len_peak);
peakFreq = zeros(1,len_freq);

for i=1:len_peak

    peakAmp(i) = max(peakAmplitudes{i});
    index = peakAmplitudes{i}==peakAmp(i);
    peakFreq(i) = peakFrequencies{i}(index);

end

end

```

### iv. Range Calculation

```

function [range] = Range_(beat_frequency, fftData, param)

Fi = beat_frequency;

range = (param.c/(2*param.slope)) .* Fi;

```

```

f = (0:param.numSamplesperChirp-1)*param.adcSamplingrate/param.numSamplesperChirp;
r = param.c/(2*param.slope) .* f;
figure
plot(r,abs(fftData(30,:)))
title('Range Vs Target Range')
grid on
xlabel('Range(m)')
ylabel('Signal Amplitude')

end

```

## v. Range bin Selection

```

function [rangebin, databin] = rangeBin_(target_range, fftData, cplxData, param)

%range resolution calculation
rng = target_range;
indexx = zeros(1,param.numChirps);

if param.rangeresol >= param.peak2peakChest
    %resolution is bigger than one rangebin
    for i=1:param.numChirps
        index_(i) = floor(rng(i)/param.rangeresol);
    end

    index = mode(index_);

    for i=1:param.numChirps
        rangebin(1,i) = fftData(i,index);
        databin(1,i) = cplxData(i,index);
    end

else

    %resolution is not bigger than one rangebin
    for i=1:param.numChirps
        indexx(1,i) = floor(rng(i)/param.rangeresol);
    end

    minIndex = min(indexx);

    coveredBins = ceil(param.peak2peakChest/param.rangeresol);
    index = minIndex + coveredBins;

    %rangebin from minIndex-index from up to down into the opposite

```

```

for i=1:param.numChirps

    for j=minIndex:indexx
        rangebin(j-(minIndex-1),i) = fftData(i,j);
        databin(j-(minIndex-1),i) = cplxData(i,j);
    end
end

end

end
end

```

## vi. Phase Extraction

```

function [phi, range]=extendedDACMalgorithm_(dataBin, param)

    I = real(dataBin);
    Q = imag(dataBin);

    phi_previous = 0;

    for k=2:length(dataBin)

        phi(k)=phi_previous + (I(k-1)*Q(k) - I(k)*Q(k-1));
        range(k) = param.c/(4*pi*param.centerFrequency) * phi(k);
        phi_previous = phi(k);

    end

    len = length(range);
    t = (0:len-1)*param.slowTime/len;

    figure
    plot(t, phi)
    xlim([param.startsec param.endsec])
    title("Phase vs Slow time")
    xlabel('time(s)')
    ylabel('phase amplitude')

end

```

## vii. Phase Difference



```

function [phi_new]=phaseDifference(phase,param)

len = length(phase);
for i=2:len
    phi_new(i)=phase(i)-phase(i-1);
end

phi_new = phi_new/max(phi_new);

len = length(phi_new);
t = (0:len-1)*param.slowTime/len;
figure
plot(t,phi_new)
xlim([param.startsec param.endsec])
title ("Differential Phase")
xlabel("time(s)")
ylabel("normalized amplitude")

end

```

### viii. Impulse Noise Removal

```

function [signal]=ImpulseDenoise(signal,param)

len = length(signal);
meanSig = mean(signal);
strd = std(signal);

N = param.samplerange;
t = linspace(param.startsec,param.endsec,N);
figure
subplot(2,1,1)
plot(t,signal,'b');
title("Phase Signal")
xlabel("time(sec)")

for i=2:len-1

    b = signal(i)-signal(i-1);
    f = signal(i)-signal(i+1);
    mean_ = (signal(i-1)+signal(i+1))/2;

    if(abs(b)>meanSig+2*strd || abs(f)>4*meanSig+2*strd)

        signal(i) = mean_/2;
    end
end

```

```

end

end

subplot(2,1,2)
plot(t,signal,'r');
title("Impulse deNoised Phase Signal")
xlabel("time(sec)")

end

```

## ix. Filter Design

```

function [filterBR, filterHR] = filterDesign_(param)

% Elliptic Bandpass filter designed using FDESIGN.BANDPASS.

match = 'both'; % Band to match exactly

% Construct an FDESIGN object and call its ELLIP method.
hBR = fdesign.bandpass(param.BFstop1, param.BFpass1, param.BFpass2, param.BFstop2, param.BAstop1, param.BApass, ...
    param.BAstop2, param.Fs);
hHR = fdesign.bandpass(param.HFstop1, param.HFpass1, param.HFpass2, param.HFstop2, param.HAstop1, param.HApass, ...
    param.HAstop2, param.Fs);
filterBR = design(hBR, 'ellip', 'MatchExactly', match);
filterHR = design(hHR, 'ellip', 'MatchExactly', match);

end

```

## x. Autocorrelation based Estimation

```

function [brEst, hrEst] = autoEstimation(br_signal,hr_signal,param)

b_cut = br_signal;
h_cut = hr_signal;

bauto = xcorr(b_cut);
hauto = xcorr(h_cut);

[bpeaks,~] = findpeaks(bauto);
[hpeaks,~] = findpeaks(hauto);

brEst = (length(bpeaks)/2) * 60/(param.endsec - param.startsec);
hrEst = (length(hpeaks)/2) * 60/(param.endsec - param.startsec);

N = param.samplerange;

```

```

t = linspace(param.startsec,param.endsec,N);
figure
subplot(2,1,1)
plot(t,bauto(1:N))
title("Autocorrelated Breathing Signal")

end

```

## xi. CS based Signal Reconstruction

```

function [recSig, peakFreqs, peakLocs]=signalReconstruction_(signal,param,iteration)

if ~exist('iteration','var')
    % third parameter does not exist, so default it to something
    iter = 2;
else
    iter = iteration;
end

signal = signal';
N = param.samplerange;
K = round(2/3 * N);
n = 0:N-1;
t = linspace(param.startsec,param.endsec,N);
Fs = param.Fs;
f = (0:N-1)*Fs/N;

%Fourier transform matrix Representation basis
psi = dfmtx(N);
psi_inv = conj(psi)/N;
signal_fft = psi*signal;

% Obtain measurements
meas = randperm(N);
meas = meas(1:K);

% sensing basis
A = psi_inv(meas,:);
y = A*signal_fft;

[recSig_fft] = OMP_(A,y,iter);

%IFFT of FFT_recSig
recSig = real(psi_inv*recSig_fft);

signal_fft = signal_fft(1:N/2+1);
recSig_fft = recSig_fft(1:N/2+1);

```

```

f = f(1:N/2+1);

[peakFreqs, peakLocs] = findpeaks(abs(recSig_fft),f);

figure;
subplot(4,1,1)
plot(t,signal)
title("Original Signal")
xlabel("time(s)")

subplot(4,1,2)
plot(f,abs(signal_fft))
title("Original Signal FFT")
% xlim([0 param.Fs/2])
xlabel("Frequency(Hz)")

subplot(4,1,3)
plot(f,abs(recSig_fft))
title("Reconstructed Signal FFT")
% xlim([0 Fs/2])
xlabel("Frequency(Hz)")

subplot(4,1,4)
plot(t,recSig)
title("Reconstructed Time Signal")
xlabel("time(s)")

figure
title("Signal Reconstruction CS-OMP")
subplot(2,1,1)
plot(t,signal,"b")
hold on
plot(t,recSig,'r',LineWidth=1)
legend("Original Signal","CS-OMP Reconstructed Signal")
xlabel("time(s)")
hold off
subplot(2,1,2)
plot(f,abs(signal_fft),'b')
hold on
plot(f,abs(recSig_fft),'r',LineWidth=1)
legend("Original Signal FFT","CS-OMP Reconstructed Signal FFT")
xlabel("Frequency(Hz)")

end

```

## xii. Wavelet Decomposition

```
function [peakAmp, maxFreq]=waveletTrial(signal,param)
```

```

len = length(signal);
level = 5;

[C,L] = wavedec(signal,level,'db5');
D1 = wrcoef('d',C,L,'db5',1);
D2 = wrcoef('d',C,L,'db5',2);
D3 = wrcoef('d',C,L,'db5',3);
D4 = wrcoef('d',C,L,'db5',4);
D5 = wrcoef('d',C,L,'db5',5);

D1 = wdenoise(D1,"wavelet","db5");
D2 = wdenoise(D2,"wavelet","db5");
D3 = wdenoise(D3,"wavelet","db5");
D4 = wdenoise(D4,"wavelet","db5");
D5 = wdenoise(D5,"wavelet","db5");

[f,signal_fft] = FFT(signal,param);
[f1,D1_fft] = FFT(D1,param);
[peakAmp{1}, maxFreq{1}] = findpeaks(D1_fft,f1);
[f2,D2_fft] = FFT(D2,param);
[peakAmp{2}, maxFreq{2}] = findpeaks(D2_fft,f2);
[f3,D3_fft] = FFT(D3,param);
[peakAmp{3}, maxFreq{3}] = findpeaks(D3_fft,f3);
[f4,D4_fft] = FFT(D4,param);
[peakAmp{4}, maxFreq{4}] = findpeaks(D4_fft,f4);
[f5,D5_fft] = FFT(D5,param);
[peakAmp{5}, maxFreq{5}] = findpeaks(D5_fft,f5);

N = param.samplerange;
t = linspace(param.startsec,param.endsec,N);

figure
subplot(6,2,1)
plot(t,signal,'k')
title('signal')
xlabel("time(s)")

subplot(6,2,2)
plot(f,signal_fft,'k')
title('signal fft')
xlabel("frequency(Hz)")

subplot(6,2,3)
plot(t,D5,'b')
title('D^5')
xlabel("time(s)")

```

```

subplot(6,2,4)
plot(f5,D5_fft,'b')
title('D^5 fft')
xlabel("frequency(Hz)")

subplot(6,2,5)
plot(t,D4,'b')
title('D^4')
xlabel("time(s)")

subplot(6,2,6)
plot(f4,D4_fft,'k')
title('D^4 fft')
xlabel("frequency(Hz)")

subplot(6,2,7)
plot(t,D3,'r')
title('D^3')
xlabel("time(s)")

subplot(6,2,8)
plot(f3,D3_fft,'k')
title('D^3 fft')
xlabel("frequency(Hz)")

subplot(6,2,9)
plot(t,D2,'b')
title('D^2')
xlabel("time(s)")

subplot(6,2,10)
plot(f2,D2_fft,'k')
title('D^2 fft')
xlabel("frequency(Hz)")

subplot(6,2,11)
plot(t,D1,'r')
title('D^1')
xlabel("time(s)")

subplot(6,2,12)
plot(f1,D1_fft,'k')
title('D^1 fft')
xlabel("frequency(Hz)")

```

```
end
```